The Astrophysical Journal, 896:102 (18pp), 2020 June 20 https://doi.org/10.3847/1538-4357/ab9308
© 2020. The Author(s). Published by the American Astronomical Society.
OPEN ACCESS

# Magnetorotational Explosion of a Massive Star Supported by Neutrino Heating in General Relativistic Three-dimensional Simulations

Takami Kuroda[1], Almudena Arcones[1,2], Tomoya Takiwaki[3], and Kei Kotake[4]
[1] Institut für Kernphysik, Technische Universität Darmstadt, Schlossgartenstrasse 2, D-64289 Darmstadt, Germany
[2] GSI Helmholtzzentrum für Schwerionenforschung, Planckstrasse 1, D-64291 Darmstadt, Germany
[3] Division of Science, National Astronomical Observatory of Japan, 2-21-1, Osawa, Mitaka, Tokyo, 181-8588, Japan
[4] Department of Applied Physics & Research Institute of Stellar Explosive Phenomena, Fukuoka University, 8-19-1, Jonan, Nanakuma, Fukuoka, 814-0180, Japan
*Received 2020 March 4; revised 2020 May 11; accepted 2020 May 12; published 2020 June 17*

## Abstract

We present results of three-dimensional (3D), radiation-magnetohydrodynamics (MHD) simulations of core-collapse supernovae in full general relativity (GR) with spectral neutrino transport. In order to study the effects of the progenitor's rotation and magnetic fields, we compute three models, where the precollapse rotation rate and magnetic fields are included parametrically to a 20 $M_\odot$ star. While we find no shock revival in our two nonmagnetized models during our simulation times (∼500 ms after bounce), the magnetorotational (MR) driven shock expansion immediately initiates after bounce in our rapidly rotating and strongly magnetized model. We show that the expansion of the MR-driven flows toward the polar directions is predominantly driven by the magnetic pressure, whereas the shock expansion toward the equatorial direction is supported by neutrino heating. Our detailed analysis indicates that the growth of the so-called kink instability may hinder the collimation of jets, resulting in the formation of broader outflows. Furthermore, we find a dipole emission of lepton number, only in the MR explosion model, whose asymmetry is consistent with the explosion morphology. Although it is similar to the lepton number emission self-sustained asymmetry (LESA), our analysis shows that the dipole emission occurs not from the proto–neutron star convection zone but from above the neutrino sphere, indicating that it is not associated with the LESA. We also report several unique neutrino signatures, which are significantly dependent on both the time and the viewing angle, if observed, possibly providing rich information regarding the onset of the MR-driven explosion.

*Unified Astronomy Thesaurus concepts:* Core-collapse supernovae (304); Magnetohydrodynamical simulations (1966); Supernova neutrinos (1666); Supernova dynamics (1664); Radiative magnetohydrodynamics (2009)

## 1. Introduction

The best-studied mechanism to explode massive stars ($\gtrsim 8 M_\odot$) is the neutrino mechanism (Bethe & Wilson 1985; Wilson 1985), where neutrinos emitted from the proto–neutron star (PNS) heat the matter behind the stalled bounce shock, leading to the shock revival into explosion, i.e., the onset of core-collapse supernovae (CCSNe; see Kotake et al. 2012; Burrows 2013; Foglizzo et al. 2015; Janka et al. 2016; Müller 2016; Radice et al. 2018, for reviews). However, the neutrino mechanism generally fails in spherically symmetric (1D) simulations (e.g., Liebendörfer et al. 2001; Sumiyoshi et al. 2005) except for super-AGB stars (Kitaura et al. 2006) that cover the low-mass end of CCSN progenitors.

Multidimensional (multi-D) hydrodynamics has dramatic impacts on the neutrino mechanism (see, e.g., Melson et al. 2015; Lentz et al. 2015; Takiwaki et al. 2016; Müller et al. 2017; O'Connor & Couch 2018; Ott et al. 2018; Pan et al. 2018; Summa et al. 2018; Burrows et al. 2019; Vartanyan et al. 2019b). Multi-D instabilities such as neutrino-driven convection and the standing accretion shock instability (SASI; Foglizzo et al. 2006; Scheck et al. 2006) increase the dwell time of matter in the postshock region, which substantially enhances the neutrino heating efficiency behind the shock. Turbulence also plays a key role, providing the pressure support and energy transport in the postshock region (e.g., Abdikamalov et al. 2015; Couch & Ott 2015; Müller & Janka 2015; Roberts et al. 2016; Takiwaki et al. 2016; Radice et al. 2018; Burrows et al. 2019; Nagakura et al. 2019). Other possible candidates to foster the onset of neutrino-driven explosions include inhomogenities in the progenitor's burning shells (e.g., Couch & Ott 2015; Müller et al. 2017; Yoshida et al. 2019), PNS convection (see, e.g., Powell & Müller 2019; Nagakura et al. 2020), updates in neutrino opacities (e.g., Bollig et al. 2017; Kotake et al. 2018), sophistication of neutrino transport schemes (e.g., Sumiyoshi & Yamada 2012; Just et al. 2018; Nagakura et al. 2019), and rotation and magnetic fields. We focus on the final facet in this paper.

A number of effects of rotation in full 3D were first studied by Fryer & Warren (2004), in which they explored the rotational effects on, e.g., the rotational instabilities, magnetic field amplification, and explosion dynamics. Positive effects of rotation in favor of the onset of explosion include the larger shock radius due to the centrifugal force (Nakamura et al. 2014), vigorous spiral SASI activity (Summa et al. 2018), and energy transport via the rotational instability (Takiwaki et al. 2016). On the other hand, rotation weakens the explodability because it results in a more extended and cooler PNS, which reduces the neutrino luminosities and energies (Marek & Janka 2009). These studies show that the impact of rotation on the neutrino mechanism depends sensitively on the precollapse rotation rate. Supported by the outcomes from these state-of-the-art multi-D simulations, we are now reaching a broad consensus that the multi-D neutrino mechanism is the most

Original content from this work may be used under the terms of the Creative Commons Attribution 4.0 licence. Any further distribution of this work must maintain attribution to the author(s) and the title of the work, journal citation and DOI.

promising way to account for canonical CCSNe with explosion energies of the order of $10^{51}$ erg ($\equiv$1 Bethe, 1 B in short) or less.

The neutrino mechanism, however, is likely to fail in a subclass of CCSNe with very energetic explosion of $\sim$10 B, which is termed as a hypernova (HN; Iwamoto et al. 1998). Observationally an HN is associated with the collapse of a very massive star typically with $\gtrsim$30–40$M_\odot$ in the main-sequence stage (Tanaka et al. 2009). The magnetorotational (MR) driven mechanism originally proposed in the 1970s (Bisnovatyi-Kogan 1970; LeBlanc & Wilson 1970; Meier et al. 1976; Müller & Hillebrandt 1979) has received considerable attention. The MR explosion mechanism relies on the extraction of the rotational free energy from the central compact objects via the magnetic fields (see also Blandford & Znajek 1977; McKinney 2006, in various contexts).

Rapid rotation of the iron core is a necessary condition for the working of the MR mechanism (see Kotake et al. 2006 for collective references of early studies therein). In the collapsing core, the magnetic fields are amplified to dynamically relevant field strengths by rotational winding and/or magnetorotational instability (MRI; Akiyama et al. 2003; Obergaulinger et al. 2009; Masada et al. 2015; Rembiasz et al. 2016). After bounce, the strong magnetic pressure launches the jets along the rotational axis (Ardeljan et al. 2000; Burrows et al. 2007; Takiwaki et al. 2009; Scheidegger et al. 2010; Winteler et al. 2012; Mösta et al. 2014; Obergaulinger et al. 2014). The highly aspherical explosion is also observationally supported by the analysis of the line profiles (e.g., Maeda et al. 2008). Note that in the nonrotating progenitors, Obergaulinger et al. (2014) were the first to point out that MR-driven pressure support in the gain region (via turbulence) fosters the onset of neutrino-driven explosion. This result clearly presents evidence that implementation of sophisticated neutrino transport is needed for a quantitative study of MR-driven CCSN modeling.

In the context of purely neutrino-driven models (without magnetic fields), it becomes certain that two-dimensional (2D) simulations overestimate the explodability for a wide variety of progenitors (Hanke et al. 2012, 2013; Couch 2013; Dolence et al. 2013; Takiwaki et al. 2014). In order to correctly capture the evolution and dynamics of the postshock turbulence, three-dimensional (3D) modeling is required. The higher explodability in 2D is also reported in MR models. Mösta et al. (2014) have shown that a full 3D model leads to the formation of the less collimated (bipolar) jets than those in the counterpart octant symmetry model, which mimics 2D. They pointed out that the less collimated outflow in 3D is an outcome of the so-called $|m| = 1$ kink instability (Begelman 1998; Lyubarskii 1999; Narayan et al. 2009). It has been demonstrated that the kink instability displaces the jet center from the rotational axis and prevents the magnetic field amplification preferentially on the axis (see also Li 2000). More recently, Obergaulinger & Aloy (2020) have reported the first 3D special relativistic magnetohydrodynamics (MHD) simulations with spectral neutrino transport. Their 3D models showed slightly longer explosion times, although the explosion energy and ejecta mass were higher and larger, respectively, compared to those in the counterpart 2D models. Any remarkable nonaxisymmetic instabilities, including the kink instability, were not seen in the 3D models of Obergaulinger & Aloy (2020), which is in contrast with Mösta et al. (2014). Therefore, the multi-D effects in MHD models are still controversial, due partly to the limited number of full 3D MHD CCSN simulations reported so far (Mikami et al. 2008; Scheidegger et al. 2010; Mösta et al. 2014; Obergaulinger & Aloy 2020).

In this paper, we report first results of full 3D–GR, MR core-collapse simulations of a 20 $M_\odot$ star with spectral neutrino transport. We calculate three models: rotating magnetized, rotating nonmagnetized, and nonrotating nonmagnetized. Our results show that the MR explosion occurs in the rotating magnetized model shortly after core bounce, whereas the shock revival is not obtained in both nonmagnetized models during our simulation time ($\sim$500 ms after bounce). While our results basically confirm the previous results (Mösta et al. 2014), our findings include detailed analysis of the kink instability, the dipole emission of lepton number in the MR explosion, and the neutrino signals from the 3D–GR MHD models with self-consistent neutrino transport.

This paper is organized as follows. Section 2 starts with a concise summary of our GR MHD neutrino transport scheme, which is followed by the initial setup of the simulation. The main results and detailed comparison with previous studies are presented in Section 3. We summarize our results and conclusions in Section 4. Note that the geometrized unit is used in Section 2, i.e., the speed of light, the gravitational constant, and the Planck constant are set to unity, $c = G = h = 1$, and cgs units are used in Section 3. The metric signature is $(-, +, +, +)$. Greek indices run from 0 to 3 and Latin indices from 1 to 3, except $\nu$ and $\varepsilon$ denoting neutrino species and energy, respectively. We also use a conventional expression for spatial coordinates $(x^1, x^2, x^3) = (x, y, z)$.

## 2. Numerical Methods and Computational Setup

In our full GR radiation-MHD simulations, we solve the evolution equations of metric, MHD, and energy-dependent neutrino radiation. Each of the evolution equations is solved in an operator-splitting manner, while the system evolves self-consistently as a whole, satisfying the Hamiltonian and momentum constraints (Kuroda et al. 2012, 2014, 2016b).

### 2.1. Basic ν-GRMHD Equations

Regarding the metric evolution, we evolve the standard BSSN variables $\tilde{\gamma}_{ij}$, $w(=e^{-2\phi})$ (Marronetti et al. 2008), $\tilde{A}_{ij}$, $K$, and $\tilde{\Gamma}^i$ (Shibata & Nakamura 1995; Baumgarte & Shapiro 1999). Here $\phi \equiv \ln(\gamma)/12$ with $\gamma = \det(\gamma_{ij})$. The gauge is specified by the "1+log" lapse and by the Gamma-driver-shift condition. Evolution equations of these variables are solved with a fourth-order finite-difference scheme in space (Zlochower et al. 2005) and with a fourth-order Runge–Kutta time integration. In the Appendix, we show results of the polarized Gowdy wave test (Alcubierre et al. 2004) to show the fourth-order convergence of our metric solver.

In the radiation-MHD part, the total stress-energy tensor $T^{\alpha\beta}_{(\mathrm{total})}$ is expressed as

$$T^{\alpha\beta}_{(\mathrm{total})} = T^{\alpha\beta}_{(\mathrm{matter})} + T^{\alpha\beta}_{(\mathrm{EM})} + \sum_{\nu\in\nu_e,\bar{\nu}_e,\nu_x} \int d\varepsilon T^{\alpha\beta}_{(\nu,\varepsilon)}, \quad (1)$$

where $T^{\alpha\beta}_{(\mathrm{matter})}$, $T^{\alpha\beta}_{(\mathrm{EM})}$, and $T^{\alpha\beta}_{(\nu,\varepsilon)}$ are the stress-energy tensor of matter, electromagnetic, and energy ($\varepsilon$) dependent neutrino radiation field of species $\nu$, respectively. We consider all three flavors of neutrinos ($\nu_e$, $\bar{\nu}_e$, $\nu_x$), with $\nu_x$ representing heavy-lepton neutrinos (i.e., $\nu_\mu$, $\nu_\tau$, and their antiparticles). $\varepsilon$

represents the neutrino energy measured in the comoving frame. In this paper, although we omit to describe detailed evolution equations of the neutrino radiation field (we refer the reader to Kuroda et al. 2016b), we solve spectral neutrino transport of the zeroth- and first-order radiation momenta, based on the truncated moment formalism (Shibata et al. 2011) employing an M1 analytical closure scheme.

In the following, we briefly describe our GR MHD formulation. The stress-energy tensor of electromagnetic field $T^{\alpha\beta}_{(\mathrm{EM})}$ is expressed as

$$T^{\alpha\beta}_{(\mathrm{EM})} = F^{\alpha\delta}F^{\beta}_{\delta} - \frac{1}{4}g^{\alpha\beta}F_{\delta\gamma}F^{\delta\gamma}, \tag{2}$$

where $F^{\alpha\beta}$ is the electromagnetic field tensor. Since we currently consider the ideal MHD case, Maxwell's equations are written in terms of the dual tensor $F^{*}_{\alpha\beta} = \frac{1}{2}\epsilon_{\alpha\beta\gamma\delta}F^{\gamma\delta}$ as

$$\nabla_{\beta}F^{*\beta}_{\alpha} = 0. \tag{3}$$

We define the magnetic field four-vector $b^{\alpha}$ as

$$b^{\alpha} = -\frac{1}{2}\epsilon^{\alpha\beta\gamma\delta}u_{\beta}F_{\gamma\delta}, \tag{4}$$

with $\epsilon^{\alpha\beta\gamma\delta}$ and $u_{\alpha}$ being the Levi–Civita tensor and matter four-velocity, respectively. In addition, for later convenience, the magnetic field three-vector $B^{i}$ should also be introduced as

$$B^{i} \equiv F^{*it} = -\gamma^{i}{}_{j}n_{\mu}F^{*j\mu} = Wb^{i} - \alpha b^{t}u^{i}, \tag{5}$$

where $W = -u^{\mu}n_{\mu}$ is the Lorentz factor (do not confuse with $w = e^{-2\phi}$ of geometrical variables) and $n_{\mu} = (-\alpha, 0, 0, 0)$ is a unit vector normal to the spacelike hypersurface foliated into the spacetime. Then, using the orthogonality condition $B^{\alpha}n_{\alpha} = 0$, the time and spatial components of Equation (3) can be rewritten as

$$\partial_{i}(\sqrt{\gamma}B^{i}) = 0, \tag{6}$$

i.e., the solenoidal constraint of $B^{i}$, and

$$\partial_{t}(\sqrt{\gamma}B^{i}) + \partial_{j}\sqrt{\gamma}(v^{j}B^{i} - B^{j}v^{i}) = 0, \tag{7}$$

respectively, where $v^{i} \equiv u^{i}/u^{t}$.

Additionally to the evolution Equation (7) of the magnetic field, we solve the following ideal hydrodynamic equations (see, e.g., Gammie et al. 2003; Shibata & Sekiguchi 2005) including electron number conservation:

$$\partial_{t}\rho_{*} + \partial_{i}(\rho_{*}v^{i}) = 0, \tag{8}$$

$$\begin{aligned}\partial_{t}\sqrt{\gamma}S_{i} + \partial_{j}\sqrt{\gamma}(S_{i}v^{j} + \alpha P_{\mathrm{tot}}\delta^{j}_{i} - \alpha B^{j}(B_{i} + B^{k}u_{k}u_{i})/W^{2}) \\ = -\sqrt{\gamma}[S_{0}\partial_{i}\alpha - S_{k}\partial_{i}\beta^{k} - 2\alpha S^{k}_{k}\partial_{i}\phi \\ + \alpha e^{-4\phi}(S_{jk} - P_{\mathrm{tot}}\gamma_{jk})\partial_{i}\tilde{\gamma}^{jk}/2 + \alpha\int d\varepsilon\sum_{\nu}S^{\mu}_{(\nu,\varepsilon)}\gamma_{i\mu}\Big],\end{aligned} \tag{9}$$

$$\begin{aligned}\partial_{t}\sqrt{\gamma}\tau + \partial_{i}\sqrt{\gamma}(\tau v^{i} + P_{\mathrm{tot}}(v^{i} + \beta^{i}) - \alpha B^{j}B^{k}u_{k}/W) \\ = \sqrt{\gamma}[\alpha K S^{k}_{k}/3 + \alpha e^{-4\phi}(S_{ij} - P_{\mathrm{tot}}\gamma_{ij})\tilde{A}^{ij} \\ - S_{i}D^{i}\alpha + \alpha\int d\varepsilon\sum_{\nu}S^{\mu}_{(\nu,\varepsilon)}n_{\mu}\Big],\end{aligned} \tag{10}$$

and

$$\partial_{t}(\rho_{*}Y_{e}) + \partial_{i}(\rho_{*}Y_{e}v^{i}) = \sqrt{\gamma}\alpha m_{\mathrm{u}}\int\frac{d\varepsilon}{\varepsilon}(S^{\mu}_{(\nu_{e},\varepsilon)} - S^{\mu}_{(\bar{\nu}_{e},\varepsilon)})u_{\mu}, \tag{11}$$

where $\rho_{*} = \rho\sqrt{\gamma}W$, $S_{i} = (\rho h + b^{2})Wu_{i} - \alpha b^{t}b_{i}$, $S_{ij} = (\rho h + b^{2})u_{i}u_{j} + P_{\mathrm{tot}}\gamma_{ij} - b_{i}b_{j}$, $S^{k}_{k} = \gamma^{ij}S_{ij}$, $\tau = S_{0} - \rho W$, and $S_{0} = (\rho h + b^{2})W^{2} - P_{\mathrm{tot}} - (\alpha b^{t})^{2}$. On the right-hand side of Equation (10), $D^{i}$ represents the covariant derivative with respect to the three-metric $\gamma_{ij}$. $\rho$ is the rest mass density, and $h = 1 + e_{\mathrm{mat}} + P_{\mathrm{mat}}/\rho$ is the specific enthalpy of matter (composed of baryons, electrons, and photons), with $e_{\mathrm{mat}}$ and $P_{\mathrm{mat}}$ being the specific internal energy and pressure of matter, respectively. $b^{2} = b^{\alpha}b_{\alpha}$, $P_{\mathrm{tot}} = P_{\mathrm{mat}} + P_{\mathrm{mag}}$ is the total pressure, $P_{\mathrm{mag}} = b^{2}/2$ is the magnetic pressure, $Y_{e} \equiv n_{e}/n_{b}$ is the electron fraction ($n_{e}$ and $n_{b}$ are the number densities of electrons and baryons, respectively), and $m_{\mathrm{u}}$ is the atomic mass unit. $P_{\mathrm{mat}}(\rho, s, Y_{e})$ and $e_{\mathrm{mat}}(\rho, s, Y_{e})$ are given by an equation of state (EOS), with $s$ denoting the entropy per baryon.

We thus evolve the following MHD and radiation conservative variables:

$$\boldsymbol{Q} = \begin{bmatrix}\rho^{*}\\ \sqrt{\gamma}S_{i}\\ \sqrt{\gamma}\tau\\ \sqrt{\gamma}B^{i}\\ \rho^{*}Y_{e}\\ \sqrt{\gamma}E_{(\nu,\varepsilon)}\\ \sqrt{\gamma}F_{(\nu,\varepsilon)_{i}}\end{bmatrix}, \tag{12}$$

where $(E_{(\nu,\varepsilon)}, F_{(\nu,\varepsilon)_{i}})$ are the zeroth- and first-order moments of neutrino radiation (Shibata et al. 2011; Kuroda et al. 2016b).

Every time we update the conservative variables $\boldsymbol{Q}$, we obtain the following primitive variables:

$$\boldsymbol{P} = \begin{bmatrix}\rho\\ u^{i}\\ s\\ B^{i}\\ Y_{e}\\ E_{(\nu,\varepsilon)}\\ F_{(\nu,\varepsilon)_{i}}\end{bmatrix} \tag{13}$$

by Newton's method.

### 2.2. Constrained Transport

We solve the conservation Equations (8)–(11) using the HLL scheme (Harten et al. 1983). Meanwhile, the induction Equation (7) is solved by a constrained transport (CT) method (Evans & Hawley 1988) to satisfy the solenoidal condition Equation (6). For the CT method, we also utilize the HLL scheme when we reconstruct the electric field that will be mentioned shortly. To solve the (HLL) Riemann problem, we need to evaluate the left and right states at cell surface. The left and right states are interpolated from cell-centered primitive variables $\boldsymbol{P}$ and some of the metric terms ($w$, $\alpha$, $\beta^{i}$, $\gamma_{ij}$), which are needed to evaluate the full conservative variables $\boldsymbol{Q}$, by a spatial reconstruction. We use the piecewise parabolic method

(PPM) for the spatial reconstruction (Colella & Woodward 1984, or Hawke et al. 2005 for a more suitable upwind reconstruction method in GR). After the spatial reconstruction step, we calculate the fastest left- and right-going wave speeds (e.g., Antón et al. 2006) and the HLL fluxes.

We also introduce the electric field $E^i$ defined by

$$\boldsymbol{E} = \sqrt{\gamma}(v \times B) \tag{14}$$

for the CT method. Then, Equation (7) can be rewritten as

$$\partial_t(\sqrt{\gamma}B^i) - (\boldsymbol{\nabla} \times E)^i = 0. \tag{15}$$

Employing a usual staggered mesh algorithm, we define the magnetic field $B^i$ and the electric field $E^i$ at cell surface and edge, respectively, while the rest of the variables are defined at cell center. For instance, $B^x$ and $E^x$ are defined at $(i + 1/2, j, k)$ and $(i, j + 1/2, k + 1/2)$, respectively, where $(i, j, k)$ denotes the cell center and, e.g., $j + 1/2$ represents a displaced position from cell center along the $y$-axis with a half-cell width. As in the usual manner, the electric field $E^i$ defined on the cell edge is obtained from the HLL flux for $B^i$, corresponding to the advection term in Equation (7). We use the nearest four electric fields defined on the cell surface, i.e., corresponding terms in the HLL flux, and take their simple arithmetic average.[5]

Our numerical grid employs a fixed nested structure, and there is a boundary between different numerical resolutions. Therefore, we apply a refluxing procedure for both the HLL fluxes and the electric field $E^i$ (Kuroda & Umeda 2010) before solving Equations (8)–(11) and (15) to satisfy the conservation law and solenoidal constraint in the whole computational domain.

### 2.3. Initial Setup

We study the frequently used solar-metallicity model of the 20 $M_\odot$ star "s20a28n" from Woosley & Heger (2007). Although one of our final aims is to understand the HN explosion mechanism of very massive stars ($\gtrsim 30 M_\odot$), this progenitor star is widely used in previous studies (e.g., Melson et al. 2015; Ott et al. 2018; O'Connor & Couch 2018; Burrows et al. 2019), and our nonrotating, nonmagnetized model (see below) could thus be a reference model to calibrate our 3D $\nu$-GRMHD code. For the nuclear EOS, we use SFHo of Steiner et al. (2013). The 3D computational domain is a cubic box with $3 \times 10^4$ km width in which nested boxes with 10 refinement levels are embedded. Each box contains $128^3$ cells, and the minimum grid size near the origin is $\Delta x = 458$ m. In the vicinity of the stalled shock at a radius of $\sim$100 km, our resolution achieves $\Delta x \sim$ 1.9 km, i.e., the effective angular resolution becomes $\sim 1^\circ$. The neutrino energy space $\varepsilon$ logarithmically covers from 1 to 300 MeV with 12 energy bins. Regarding neutrino opacities, the standard weak interaction set in Bruenn (1985), which consists of the absorption and emission process

$$\nu_e n \leftrightarrow e^- p, \tag{16}$$

$$\bar{\nu}_e p \leftrightarrow e^+ n, \tag{17}$$

$$\nu_e A \leftrightarrow e^- A', \tag{18}$$

isoenergy scattering of neutrinos off nucleons and heavy nuclei

$$\nu n \leftrightarrow \nu n, \tag{19}$$

$$\nu p \leftrightarrow \nu p, \tag{20}$$

$$\nu A \leftrightarrow \nu A, \tag{21}$$

inelastic neutrino electron scattering

$$\nu e \leftrightarrow \nu e, \tag{22}$$

and thermal neutrino pair production and annihilation

$$e^- e^+ \leftrightarrow \nu\bar{\nu}, \tag{23}$$

is taken into account. In addition, nucleon–nucleon bremsstrahlung (Hannestad & Raffelt 1998)

$$NN \leftrightarrow NN\nu\bar{\nu} \tag{24}$$

is also included (for more details, see Kuroda et al. 2016b).

The original progenitor model "s20a28n" assumes neither rotation nor magnetic fields. We thus artificially add them to the nonrotating progenitor model. We employ a widely used cylindrical rotational profile (Dimmelmeier et al. 2002)

$$u^t u_\phi = \varpi_0^2(\Omega_0 - \Omega), \tag{25}$$

where $u_\phi \equiv \varpi^2\Omega$ with $\varpi = \sqrt{x^2 + y^2}$. $\Omega$ is the angular frequency of the fluid element. Using $\Omega$, the rotational component of the initial four-velocity is simply set by $(u_x, u_y, u_z) = \Omega(y, x, 0)$. $\varpi_0$ and $\Omega_0$ indicate the size and angular frequency of a rigidly rotating central cylinder, respectively. Note that $\Omega_0$ and $\Omega$ are measured by an Eulerian observer. This rotational profile gives the angular frequency falling off with $\varpi^{-2}$ beyond $\varpi_0$, i.e., the specific angular momentum asymptotically reaches a constant value $\varpi_0^2\Omega_0$.

For the initial magnetic fields that should satisfy the solenoidal constraint, we use the following purely toroidal vector potential:

$$A_\phi = \frac{B_0}{2}\frac{R_0^3}{r^3 + R_0^3} r \sin\theta, \tag{26}$$

$$A_r = A_\theta = 0. \tag{27}$$

Here $(r, \theta, \phi)$ denote the usual coordinates in the spherical polar coordinate system. By defining these vector potentials on the cell edge and taking their curl $\boldsymbol{B} = \nabla \times \boldsymbol{A}$, the magnetic field defined on the numerical cell surface automatically satisfies the solenoidal constraint. This vector potential gives nearly uniform magnetic field parallel to the rotational axis (i.e., $z$-axis) for $r \lesssim R_0$ and dipolar magnetic field for $r \gtrsim R_0$.

We set $\varpi_0 = R_0 = 10^8$ cm corresponding roughly to the iron core size at the precollapse stage. We calculate three models: rotating magnetized, rotating nonmagnetized, and nonrotating nonmagnetized. For the rotating models, we set $\Omega_0 = 1$ rad s$^{-1}$. This value is very reasonable compared to the one of a rotating 20 $M_\odot$ model in Heger & Langer (2000) that gives $\Omega_0 \sim 3$ rad s$^{-1}$. Regarding the magnetic field strength at origin, we set $B_0 = 10^{12}$ G, which can be amplified strongly enough to affect the dynamics through simple linear amplification mechanisms, i.e., compression and rotational wrapping, during collapse and is also widely used in most of the previous MHD simulations (Burrows et al. 2007; Takiwaki et al. 2009; Scheidegger et al. 2010; Mösta et al. 2014; Obergaulinger &

[5] Although we used a simple arithmetic average in this study, we later found that the upwind reconstruction (e.g., White et al. 2016) could significantly reduce numerical oscillations seen in the reconstructed electric field, especially outside the SN shock surface where the flow is supersonic, which eventually led to the crash of current MHD simulations.

Aloy 2020). Three models are labeled as R0B00, R1B00, and R1B12, where the integer after $R$ denotes $\Omega_0$. B00 and B12 represent $B_0 = 0$ and $10^{12}$ G, respectively.

## 3. Results

In this section, we explain our main results. Sections 3.1 and 3.2 are devoted to explaining general hydrodynamic properties in the postbounce evolution. In Section 3.3, we discuss nonaxisymmetric instabilities in the PNS and MHD outflow, which is relevant to the neutrino signals in Section 3.4. The role of neutrino heating in the MR mechanism is addressed in Section 3.5. We explain the dipole emission of lepton number in our MR explosion model in Section 3.6.

### 3.1. Postbounce Evolution

We begin with a brief description of the postbounce evolution of all three models in this work. After the start of calculation ($t = 0$), the core bounce occurs at $t = 0.261$, 0.264, and 0.265 s for models R0B00, R1B00, and R1B12, respectively. The central (maximum) rest mass density $\rho_{\rm max}$ reaches $4.42 \times 10^{14}\,{\rm g\,cm^{-3}}$ (model R0B00), $4.37 \times 10^{14}\,{\rm g\,cm^{-3}}$ (R1B00), and $4.35 \times 10^{14}\,{\rm g\,cm^{-3}}$ (R1B12). A monotonic feature that rapid rotation and high initial magnetic field delay the bounce time and decrease $\rho_{\rm max}$ is due to the stronger centrifugal force and magnetic pressure at bounce. The lapse function at the center also shows a similar trend, where it takes the smallest and highest value for models R0B00 and R1B12, respectively. For the computed three models, $\rho_{\rm max}$ and the (minimum) lapse function evolve with time after bounce, keeping the above trend at bounce (e.g., smallest $\rho_{\rm max}$ for model R1B12 relative to other models).

To visualize the postbounce evolution, Figure 1 shows the volume-rendered entropy (top three panels) and inverse of the plasma $\beta$ for model R1B12 in the logarithmic scale (bottom three panels) at selected postbounce times ($t_{\rm pb}$). Here the plasma $\beta$ is defined by the ratio of the gas to the magnetic pressure, i.e., $\beta \equiv P_{\rm gas}/P_{\rm mag}$. After bounce, the formation of the bipolar flow can be clearly seen in the left panels. Inside the expanding blobs, the magnetic pressure dominates over the gas pressure as shown by the yellowish region ($\log_{10}\beta^{-1} \gtrsim 0.5$) in the bottom panels. This is a clear evidence of the MR-driven shock revival for model R1B12. As an important 3D effect, we see that the shock morphology is less collimated compared to the previous 2D axisymmetric studies, although similar initial rotation and magnetic fields were adopted (Burrows et al. 2007; Takiwaki et al. 2009; Mösta et al. 2014; Obergaulinger & Aloy 2017). The middle panels show that the jet head is not aligned with the rotational axis at $t_{\rm pb} \sim 100$ ms but is displaced from the axis (indicated by the deviation from the white line). In Section 3.3, we will discuss the reason for this in more detail.

Figure 2 shows the volume-rendered entropy structure for models R0B00 (top panels) and R1B00 (bottom panels) from $t_{\rm pb} \sim 245$–$500$ ms. Comparing with the uni-/bipolar-like structure seen in the magnetized model R1B12, the shock morphology of these two nonmagnetized models is obviously different. Models R0B00 and R1B00 show roundish and oblate shock morphology, respectively. During our simulation time up to $t_{\rm pb} \sim 500$ ms, we do not find a shock revival in these two nonmagnetized models.

### 3.2. Shock Wave Evolution

Figure 3 shows the maximum (thick lines) and averaged (thin) shock radii in the top panel and the time evolution of the diagnostic explosion energy $E_{\rm exp}$ and mass accretion rate ($\dot{M}$) in the bottom panel for models R0B00 (black line), R1B00 (blue line), and R1B12 (red line), respectively. Here $E_{\rm exp}$ is defined by

$$E_{\rm exp} = \int_{\tau>0} \sqrt{\gamma}\,\tau dx^3, \tag{28}$$

which is analogous to Equation (2) of Müller et al. (2012) but takes into account the additional contribution from magnetic fields. For the mass accretion rate, we first measure the mass flux just above the shock surface on the negative $z$-axis and positive $x$-axis and then multiply them by $4\pi R_{\rm shock}^2$. Here $R_{\rm shock}$ is the corresponding shock position. Since model R1B12 shows unipolar-like explosion mainly toward the negative $z$-axis, we show the value measured on that axis. The value on the positive $x$-axis can be considered as a typical value along the equatorial plane.

From the top panel, one can see that the shock revival is not obtained for the nonmagnetized models R0B00 (black line) and R1B00 (blue line) for the simulation time, whereas the shock propagates outward in the magnetized model R1B12 (red line). The shock is slightly energized at $t_{\rm pb} \sim 180$ ms for model R1B12 and at $t_{\rm pb} \sim 200$ ms for models R0B00/R1B00, when the Si/O interface accretes onto the shock. This leads to the runaway shock expansion for model R1B12, whereas it only results in the slight shock expansion maximally up to the radius of ∼400 km for model R1B00, gradually shifting to the standing shock later on (see blue and black lines). The time when the Si/O interface accretes onto the shock differs by about ∼20 ms between model R1B12 and the other two models. The time lag is because of the difference in the (maximum) shock position ($\sim 4 \times 10^7$ cm) at $t_{\rm pb} \sim 180$ ms. Since the typical accretion velocity is $\sim 2 \times 10^9\,{\rm cm\,s^{-1}}$ there, this can be translated into the crossing time of ∼20 ms, which is consistent with the time difference. The mass accretion rate in Figure 3 also supports this. In the bottom panel, the mass accretion rate measured on the negative $z$-axis $\dot{M}(-Z)$ for model R1B12 (red thin solid line) shows the fastest time of accretion of the Si/O interface at $T_{\rm pb} \sim 182$ ms, while it accretes at $T_{\rm pb} \sim 205$ ms in model R0B00 (black thin lines) and also along the equatorial plane in model R1B00 (blue thin dashed line, which is overlapped by the black lines). Therefore, the aforementioned shock expansion can be explained by a sudden reduction of mass accretion rate in association with the accretion of the Si/O interface.

The diagnostic explosion energy in the bottom panel basically correlates with the shock evolution. In the successful explosion model R1B12, the diagnostic explosion energy increases significantly faster than the other two nonexplosion models already at ∼20 ms after bounce. It reaches $\sim 10^{50}$ erg around $t_{\rm pb} \sim 100$ ms. The value $E_{\rm exp} \sim 10^{50}$ erg at the time when the shock reaches $R_{\rm shock} \sim 1000$ km is very similar to the ones in previous 2D (Takiwaki et al. 2009; Obergaulinger & Aloy 2017) and 3D (Obergaulinger & Aloy 2020) studies with the similar initial rotation and magnetic fields strength. In the nonmagnetized models R0B00 and R1B00, $E_{\rm exp}$ temporally reaches $\sim 10^{49}$ erg at $T_{\rm pb} \sim 220$ ms when the Si/O interface

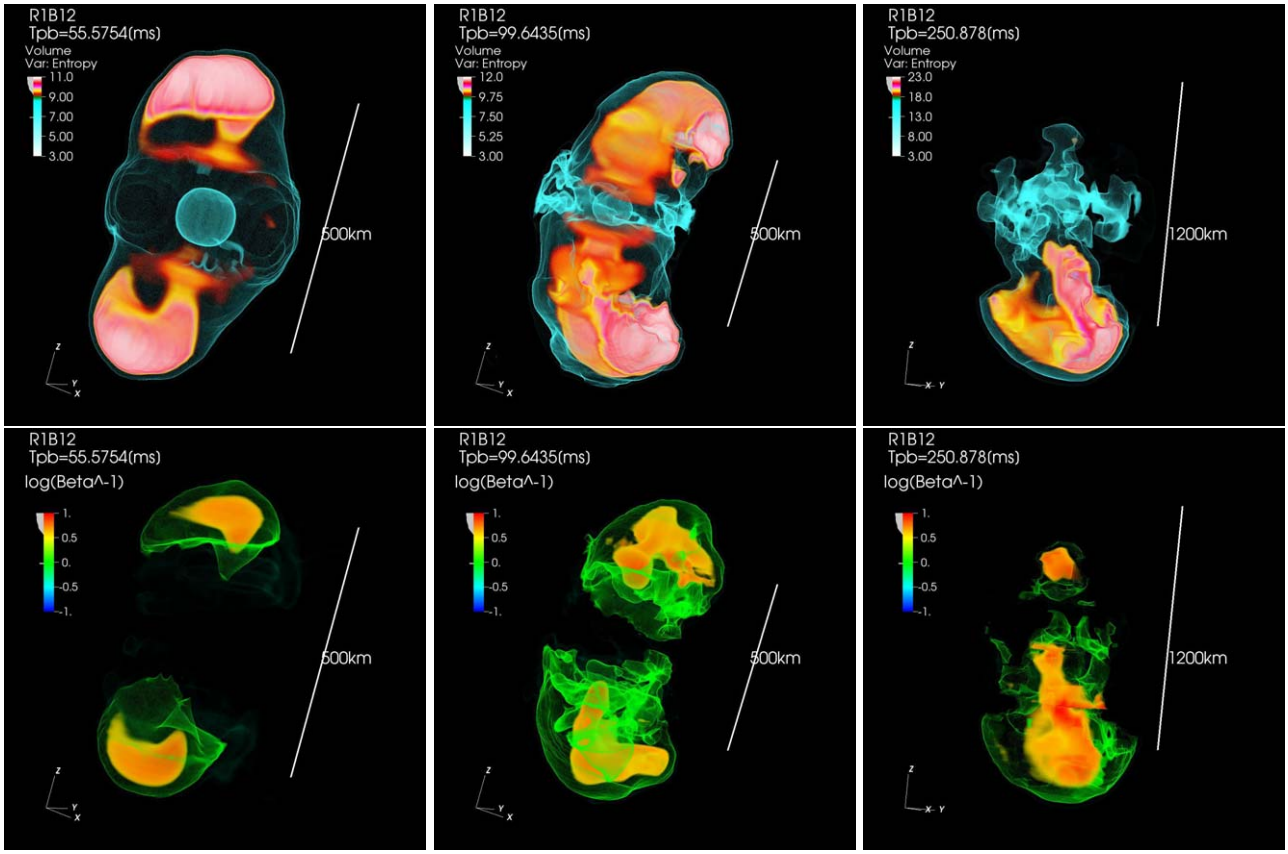


**Figure 1.** Snapshots of the volume-rendered entropy (top panels) and inverse of the plasma $\beta$ in the logarithmic scale ($\log \beta^{-1}$; bottom panels) for model R1B12. From left to right panels, the postbounce times of $t_{\rm pb} \sim 56$, 100, and 250 ms are depicted, respectively. In the top panels, the central bluish spherical/spheroidal object roughly corresponds to the unshocked PNS core. Note that the inclination angle of the coordinates is not fixed in each time snapshot to visualize the expansion morphology more clearly. The white line denotes the length scale that is parallel to the rotational axis ($z$-axis).

accretes and a temporal shock expansion occurs, though it soon decreases.

We can also find a typical signature of SASI in the evolution of shock radii. From the top panel of Figure 3, a time modulation is visible in the maximum shock radii, particularly in model R0B00 (thick black line) for $t_{\rm pb} \gtrsim 100$ ms.

Such a modulation reflects the appearance of SASI (Foglizzo et al. 2006; Scheck et al. 2006). To see more quantitatively the shock morphology and also the dominant SASI mode, we plot time evolution of normalized mode amplitudes $A_{\ell m} \equiv c_{\ell m}/c_{00}$ of spherical polar expansion of the shock surface $R_{\rm shock}(\theta, \phi)$ for several dominant modes in Figure 4. Here we adopt the same definition for $c_{\ell m}$ as in Burrows et al. (2012), with $\ell$ and $m$ representing the quantum number with respect to the real spherical harmonics of $Y_\ell^m$, respectively.

In the top panel, the dominant mode is $(\ell, m) = (2, 0)$ (black line) for the first $\sim$120 ms after bounce. Since its sign is positive, the shock morphology is prolate, as also shown in the left and center columns in Figure 1. However, for $t_{\rm pb} \gtrsim 120$ ms in the same model R1B12, $(\ell, m) = (1, 0)$ (red line) gradually takes over as the dominant term with its sign being negative. Therefore, the shock morphology at the end of simulation time is unipolar toward the negative $z$-axis, which is again consistent with the right column in Figure 1. In the middle panel, R1B00 shows that $A_{20}$ becomes negative for $t_{\rm pb} \gtrsim 50$ ms, which reflects a rotating oblate spheroid (see bottom panels in Figure 2). At the same time, $(\ell, m) = (1, \pm 1)$ (blue and green lines) also show comparable amplitudes with that of (2, 0), but with clear quasi-periodic oscillations. Between these two $|m| = 1$ modes, i.e., $(\ell, m) = (1, 1)$ and $(1, -1)$, a phase shift seemingly with $\sim\pi/2$ exists that indicates that the spiral SASI motion appears (Blondin & Mezzacappa 2007). In the nonrotating model R0B00, all three modes with $\ell = 1$ and $m = 0, \pm 1$ show basically the same amplitude with almost no phase shift up to $t_{\rm pb} \sim 120$ ms. Therefore, the dominant SASI mode is the sloshing mode first after bounce. Afterward the (1, 0) mode gradually decouples from the other two different azimuthal modes. There seems to be a phase shift of $\sim\pi/2$ between (1, 0) (red line) and the other two with $(1, \pm 1)$ (green and blue). This can be explained by the dominant SASI motion changing from the sloshing motion to the spiral one around $t_{\rm pb} \sim 120$ ms. Note that the growth of the spiral SASI in the nonrotating progenitors (Blondin & Mezzacappa 2007) is consistent with the outcomes of previous 3D core-collapse models (Hanke et al. 2013; Kuroda et al. 2016a; Ott et al. 2018).

### 3.3. Nonaxisymmetric Instabilities inside the MHD Outflow

In this subsection, we discuss nonaxisymmetric instabilities inside the MHD outflow and their potential impact on the shock evolution. In a 3D–GR model using similar precollapse rotation rate and magnetic fields to our model R1B12, Mösta et al. (2014) observed the appearance of the kink instability (Begelman 1998; Lyubarskii 1999; Narayan et al. 2009). According to their analysis, the linear growth of the kink instability shortly starts after bounce, which is followed by the nonlinear phase

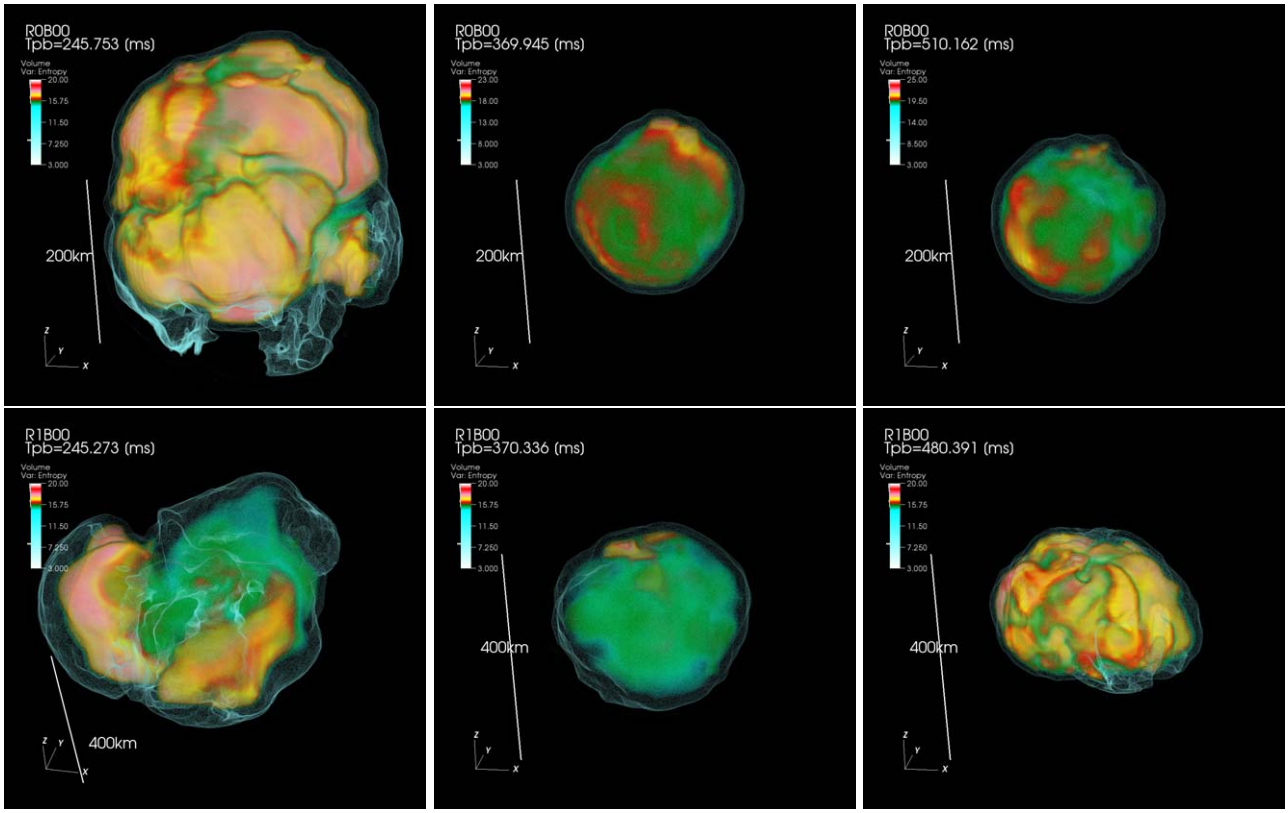


**Figure 2.** Same as Figure 1, but for only entropy of nonmagnetized models at different time slices $t_{\rm pb} \sim 245$, 370, and 500 ms. The top and bottom panels are for models R0B00 and R1B00, respectively. Note again that the white line denotes the length scale that is parallel to the rotational axis ($z$-axis).

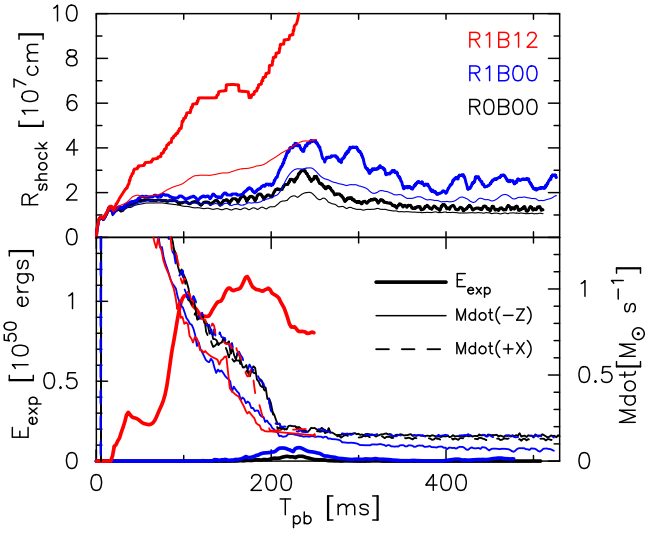


**Figure 3.** Top: maximum (thick lines) and averaged (thin) shock radii ($R_{\rm shock}$) plotted as a function of the postbounce time. Bottom: time evolution of the diagnostic explosion energy ($E_{\rm exp}$; thick lines) and the mass accretion rate ($\dot{M}$; thin solid/dashed lines) for all models. In each panel, the color indicates the model name: red (R1B12), blue (R1B00), and black (R0B00). For the mass accretion rate, we first measure the mass flux just above the shock surface on the negative $z$- and positive $x$-axes and then multiply them by $4\pi R_{\rm shock}^2$. Here $R_{\rm shock}$ is the corresponding shock position.

already at $t_{\rm pb} \sim 20$ ms. At that moment, the jet barycenter showed a significant displacement from the rotational axis, which is one of the main features of the growth of the kink instability, leading to a broader and less energetic outflow compared to the counterpart axisymmetric case. We also check whether this instability appears and affects the dynamics of outflow in model R1B12.

The condition $|b_\phi/b_z| > \varpi/L$, i.e., the well-known Kruskal–Shafranov criterion, is the major factor that determines whether the system is unstable to the most dominant screw mode, i.e., for $|m| = 1$ mode with a condition $mb_\phi < 0$. Here $L$ and $\varpi$ denote the inverse of minimal wavenumber of the unstable mode propagating parallel to the rotational axis and distance from the rotational axis, respectively. In a sufficiently rapidly rotating case, one should also take into account the rotational stabilizing effect that relaxes the Kruskal–Shafranov criterion to $|b_\phi/b_z| > \Omega\varpi$ (Tomimatsu et al. 2001), where $\Omega$ is the angular frequency in geometric units. In our magnetized model R1B12, the toroidal magnetic field dominates over the poloidal one $|b_\phi/b_z| > 1$ just above the PNS core ($z \sim 10 - 50$ km). Such a configuration is usually seen in the magnetized collapse model, as the initial poloidal field can be very efficiently converted into the toroidal one mainly through the field wrapping. As a consequence, the value $|b_\phi/b_z|/(\Omega\varpi)$ inside the MHD outflow reaches $\mathcal{O}(10^2-10^3)$ in our model. We therefore consider that the MHD outflow that appeared in our model R1B12 can also be subject to the kink instability.

Following Mösta et al. (2014), we monitor how the barycenter of MHD outflow is displaced from the rotational/magnetic field axis, i.e., $z$-axis. We take the same definition for the barycenter $x_{\rm c}^i$ written by (Mösta et al. 2014)

$$x_{\rm c}^i(z) = \frac{\int ds\, x^i\, P_{\rm mag}}{\int ds\, P_{\rm mag}}, \tag{29}$$

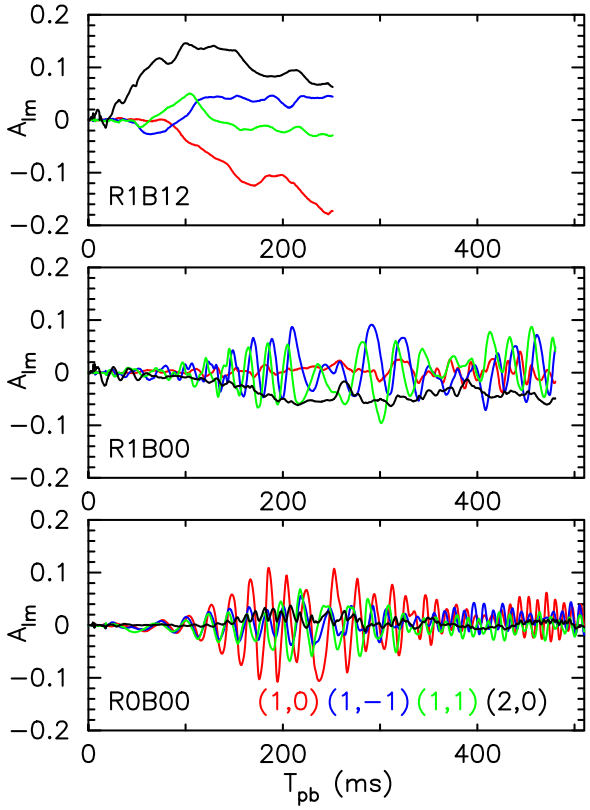


**Figure 4.** Time evolution of normalized mode amplitudes $A_{\ell m}$ of spherical polar expansion of the shock surface $R_{\rm shock}(\theta, \phi)$. The top, middle, and bottom panels are for models R1B12, R1B00, and R0B00, respectively. Note that we plot only several dominant modes, $(\ell, m) = (1, 0)$, $(1, \pm 1)$, and $(2, 0)$, denoted in the bottom panel.

for $i = 1$ and 2, where we perform the surface integral $\int ds$ over the domain with $|x, y| \leqslant 50$ km at $z = \pm 50$ km. In addition, to see the mode propagation direction properly in a rotating system, we map the original Cartesian coordinates $x^i$ to a rotating frame $\bar{x}^i$ by

$$\bar{x}^i = Q^i_j x^j, \tag{30}$$

with $Q^i_j$ being the usual rotation operator with respect to $z$-axis

$$Q^i_j = \begin{bmatrix} \cos\Theta & \sin\Theta & 0 \\ -\sin\Theta & \cos\Theta & 0 \\ 0 & 0 & 1 \end{bmatrix}. \tag{31}$$

$\Theta(t, z)$ measures the cumulative rotation angle of the system at a given slice $z(=\bar{z})$ after core bounce and is given by the following rough estimation:

$$\Theta(t, z) = \int_{t_{\rm cb}}^{t} dt'\, \bar{\omega}, \tag{32}$$

where $\bar{\omega}(t, z)$ is the mean angular frequency of the plane. Since the PNS differentially rotates, the rotational angle $\Theta(t, z)$ is just a rough measurement. We evaluate the mean angular frequency $\bar{\omega}(t, z)$ simply by

$$\bar{\omega}(t, z) = \frac{\int ds\, \omega^z\, \rho}{\int ds\, \rho}, \tag{33}$$

where $\omega^z = v^z / \sqrt{x^2 + y^2}$ is the angular frequency measured in the Eulerian frame and we use the rest mass density as a weight. After mapping, we plot the barycenter $x^i_{\rm c}$ on the rotating plane $\bar{x}\bar{y}$ at $\bar{z} = \pm 50$ km.

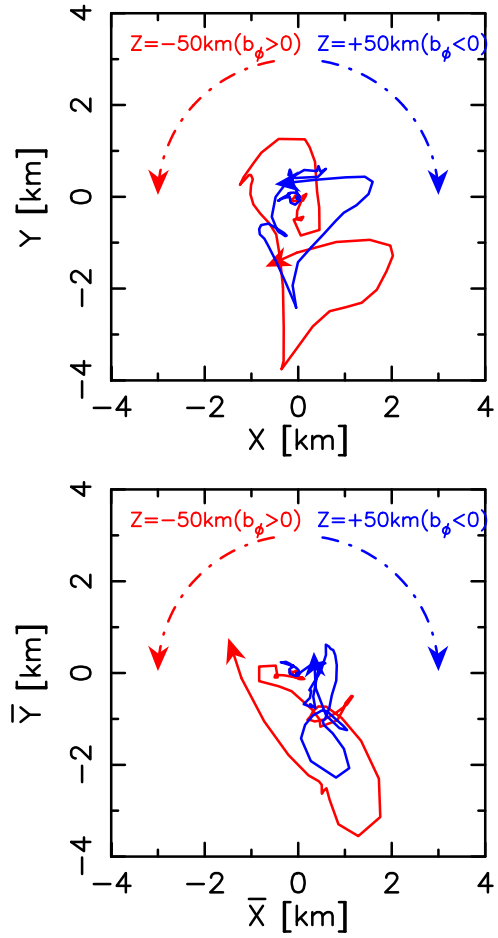


**Figure 5.** Solid lines: trajectories of the barycenter of MHD outflow on the original $x$-$y$ plane (top) and on the rotating $\bar{x}\bar{y}$ plane (bottom). The color represents the position of the planes either at $z = 50$ km (blue lines) or at $z = -50$ km (red lines). Time evolution is indicated by the arrow. Dashed −dotted lines show the direction of $b_\phi$, averaged over $\varpi \lesssim 40$ km, which is clockwise ($b_\phi < 0$) and counterclockwise ($b_\phi > 0$) for $z > 0$ and $z < 0$, respectively, on these planes.

In the top and bottom panels of Figure 5, we show the trajectory of the barycenter of MHD outflow (solid lines) on the original $xy$ and rotating $\bar{x}\bar{y}$ planes at $z = \pm 50$ km. To highlight the initial linear growth phase, we show only from the bounce time up to $t_{\rm pb} = 30$ ms, which is indicated by the arrow. In addition, we show the direction of $b_\phi$ averaged over $\varpi \lesssim 40$ km by the dashed–dotted line for reference. Because of our initial purely poloidal magnetic field with dipole-like structure orienting toward positive $z$-axis, the direction of the toroidal component generated after core collapse mainly through the field wrapping is basically clockwise ($b_\phi < 0$) and counterclockwise ($b_\phi > 0$) for $z > 0$ and $z < 0$, respectively, on these planes. Note that the positive $z$-axis points toward us, and from the condition $mb_\phi < 0$ that selects the leading mode to develop, the propagation direction of the most unstable mode in a comoving frame is expected to be counterclockwise ($m = 1$) and clockwise ($m = -1$) for $z > 0$ and $z < 0$, respectively.

From the top panel of Figure 5, both of the solid lines show a basically counterclockwise propagation direction, i.e., the $m = 1$ mode. In the top panel, the mode propagation direction

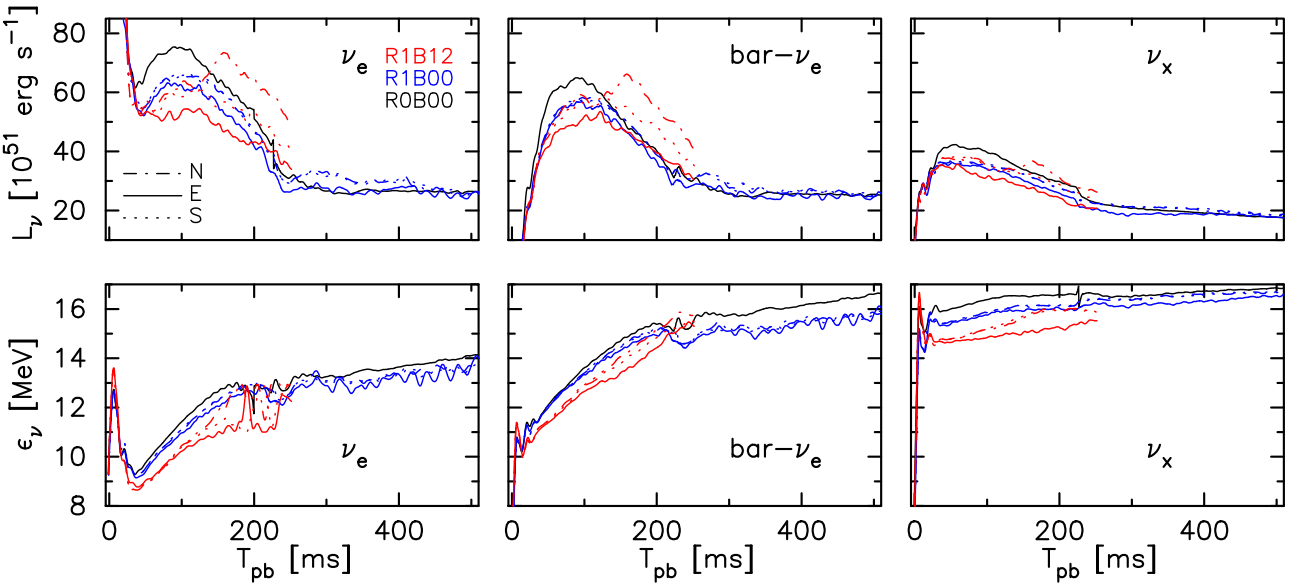


**Figure 6.** We plot (viewing-angle-dependent) neutrino luminosity $L_\nu$ (top row) and mean neutrino energy $\varepsilon_\nu$ (bottom row) at specific observer angles for $\nu_e$ (left), $\bar{\nu}_e$ (middle), and $\nu_x$ neutrinos (right). These quantities are estimated at a radius of $r = 400$ km. We choose three observer angles denoted by N (north pole), E (equatorial plane, here represented by positive $x$-axis), and S (south pole). For the nonrotating model R0B00, we plot only spherical-averaged values (solid black line) for simplicity.

(blue solid arrow) is counterclockwise (i.e., $m = 1$) and is opposite to that of $b_\phi(<0)$ (blue dashed–dotted arrow), for the region with $z > 0$, meaning that it is consistent with a linear analysis $mb_\phi < 0$. On the other hand, in the same top panel, both solid and dashed–dotted red arrows are pointing toward the same counterclockwise direction on the plane at $z = -50$ km, which is not in accordance with the theoretical expectation $mb_\phi < 0$. We think that this inconsistency seen in red arrows (top panel) is apparent, as, from the bottom panel, the red solid arrow in the rotating frame is showing a clockwise propagation direction (i.e., $m = -1$) opposite to that of $b_\phi(>0)$. These facts support that the kink instability likely appears, displaces the shock center, and consequently makes the shock morphology broader compared to the corresponding 2D model.

We should also mention another relevant nonaxisymmetric instability that might influence the growth of the above kink instability. As we have already mentioned, the ratio of rotational to gravitational potential energy after bounce in both of our rotating models reaches several percent, which makes the PNS core subject to the low-$T/W$ instability (Watts et al. 2005; Saijo & Yoshida 2006). Once the instability appears, it produces an instability mode that propagates in the same direction as the fluid motion, i.e., this time with the $m = 1$ mode in both the northern and southern hemispheres. Therefore, it means that the two different instabilities, namely, the low-$T/W$ and kink instabilities, could simultaneously exist possibly with the same $m = +1$ mode for $z > 0$ and with two opposite $m = \pm 1$ modes for $z < 0$, breaking the parity between northern and southern hemispheres.

It is beyond the scope of this paper to quantify how the two instabilities coexist, how they affect the PNS core dynamics, and the disruption of the bipolar flows as seen in model R1B12. Once the bipolar flows are disrupted, the mass accretion rate becomes higher on the weaker explosion side as a consequence of deflection of mass accretion on the stronger explosion side. This could explain a relatively weak explosion ($E_{\rm exp} \sim 10^{50}$ erg) of model R1B12. Apparently we need more studies that vary the initial magnetic fields and rotational profiles systematically in order to clarify the disruption mechanism of the MHD outflows.

### 3.4. Rotational Effects on Neutrino Profiles

The time modulation of CCSN neutrino signals reflects the hydrodynamics evolution of the postbounce core (e.g., Tamborra et al. 2013; Walk et al. 2019; and Mirizzi et al. 2016 for a review). In this section, we describe how we can make the connection between the core dynamics and neutrino signals. In Figure 6, we plot the neutrino luminosity $L_\nu$ (top row) and mean neutrino energy $\varepsilon_\nu$ (bottom row) for specific observer angles for electron type (left), antielectron type (middle), and heavy-lepton-type neutrinos (right). Here we evaluate these signals by averaging the neutrino's energy flux at $r = 400$ km following Tamborra et al. (2014). We choose three observer angles relative to the rotational axis that are denoted by N (north pole), E (equatorial plane, here represented by the positive $x$-axis), and S (south pole). To prevent too many lines, we plot only spherical-averaged values for the nonrotating model R0B00 (solid black line), as it shows basically no significant asymmetry.

Common features among all models are as follows. The neutrino luminosities of all flavors plateau at $t_{\rm pb} \sim 50$–$100$ ms. At that moment, the luminosities reach $L_\nu \sim 6 \times 10^{52}$ erg s$^{-1}$ for $\nu_e$ and $\bar{\nu}_e$ and $L_\nu \sim 3.5 \times 10^{52}$ erg s$^{-1}$ for $\nu_x$. Although such values depend on the progenitor star, EOS, and neutrino matter interactions employed, the peak luminosities are in good agreement with those in recent studies with detailed neutrino transport (Müller et al. 2017; O'Connor & Couch 2018; Summa et al. 2018; Vartanyan et al. 2019b). The luminosities become nearly constant at $t_{\rm pb} \sim 220$ ms when the mass accretion decreases suddenly. We can also see how the progenitor rotation and magnetic field affect the neutrino signals. The nonrotating model R0B00 shows basically the highest luminosity and mean energy in all flavors of neutrinos (see black lines). Meanwhile, the rotating magnetized model R1B12, which explodes shortly after bounce, shows the lowest

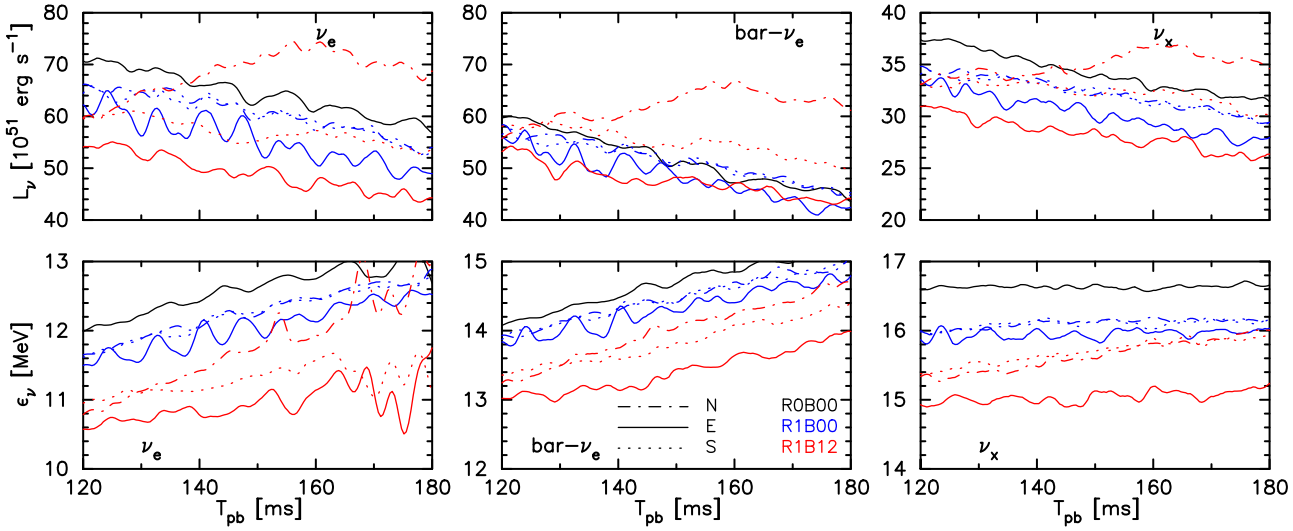


**Figure 7.** Same as Figure 6, but for the postbounce time from $t_{pb} = 120$ to 180 ms.

values in both luminosities and mean energies, though there is a slight observer angle dependence. The model R1B00 appears in between them. Such features stem from the fact that the most compact PNS of R0B00 without being subject to the rotational flattening emits higher neutrino luminosities and energies owing to its hotter core temperature. On the other hand, the rotating magnetized model R1B12, which shows a lower mass accretion rate owing to the centrifugal force and also experiences the mass ejection through bipolar outflow, has a less compact PNS, leading to lower neutrino energies and luminosities.

Next, we focus on the viewing angle dependence of the neutrino signals. In Figure 7, we show a magnified view of Figure 6 from $t_{pb} = 120$ to 180 ms. In both the rotating models R1B00 and R1B12, the neutrino luminosity and energy observed along the equatorial plane (solid red and blue lines) show the lowest value compared to those along the rotational axis (dashed–dotted and dotted lines labeled by N and S). This is because of the rotational flattening of the PNS, where the neutrino sphere radius along the equatorial plane is located outward from that of the rotational axis, making the neutrino temperature seen along the equator lower than that from the rotational axis (e.g., Kotake et al. 2003; Ott et al. 2008; Harada et al. 2019).

To show the viewing angle dependence more quantitatively, we plot the rms variation $\sqrt{\langle \delta L_\nu^2 \rangle}$ around the angle-averaged neutrino luminosities $\langle L_\nu \rangle$ in Figure 8, where $\sqrt{\langle \delta L_\nu^2 \rangle}$ is defined by

$$\sqrt{\langle \delta L_\nu^2 \rangle} \equiv \sqrt{\frac{1}{4\pi} \int_{R=400\mathrm{km}} ds \left( \frac{L_\nu - \langle L_\nu \rangle}{\langle L_\nu \rangle} \right)^2}. \quad (34)$$

As we have mentioned, the rotational flattening of the PNS produces the larger viewing angle dependence that is clearly seen by larger rms values in R1B00 than those in R0B00. Furthermore, model R1B12 shows the largest variance owing to its highly aspherical explosion morphology. Another remarkable feature is that there is a hierarchy by neutrino species of $\nu_e > \bar{\nu}_e > \nu_x$, which is most significant in model R1B12 and is diminished in nonrotating nonexploding model R0B00. We note that the hierarchy is different from the

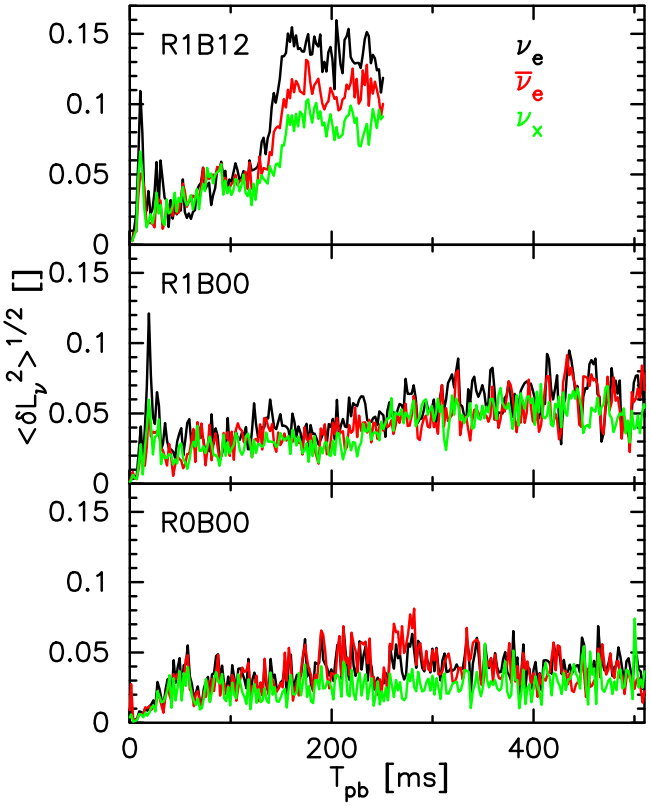


**Figure 8.** Time evolution of the rms variation $\sqrt{\langle \delta L_\nu^2 \rangle}$ around the angle-averaged neutrino luminosities for all neutrino flavors. From top to bottom, we show the value in models R1B12, R1B00, and R0B00.

previous report $\bar{\nu}_e > \nu_e > \nu_x$ by Vartanyan et al. (2019a). Although we do not know the exact reason of the difference, the hierarchy basically indicates how large each of the neutrino spheres deforms and, thus, may depend on both the adopted neutrino opacities and transport method.

There is yet another neutrino signature for model R1B00. Seen from the equatorial plane (blue solid line), a clear periodic time modulation can be seen. On the other hand, the modulation is hard to see from the rotational axis (blue dashed–dotted and dotted lines). Furthermore, the degree of the

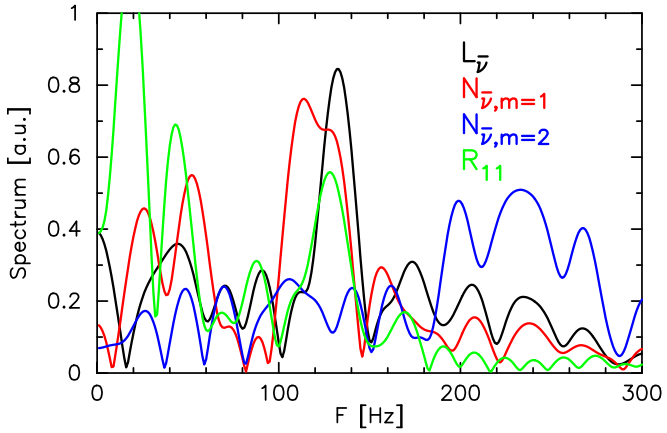


**Figure 9.** Spectra of the (viewing-angle-dependent) neutrino luminosity $L_{\bar{\nu}_e}$ (black line) corresponding to the blue solid line in the top middle panel of Figure 7; of normalized mode amplitudes of the number luminosity $N_{\bar{\nu}_e,m}$, with the lower index $m$ being the azimuthal mode either $m = 1$ (red) or $m = 2$ (blue); and of the normalized mode amplitude of spherical polar expansion of the isodensity surface $R_{11}$, extracted at the rest mass density of $\rho = 10^{11}$ g cm$^{-3}$, for $(\ell, m) = (1, 1)$ (green). The vertical axis is in arbitrary units. Here $R_{11}$ is roughly representing the neutrino sphere. The spectra are obtained by the Fourier transformation for the time interval of 120 ms $\leqslant t_{\rm pb} \leqslant$ 180 ms.

rotational effect differs depending on the neutrino flavor. It is particularly strong in $\nu_e$ and becomes weaker in order of $\bar{\nu}_e$ and $\nu_x$. Figure 7 shows that $\nu_e$ signals have a time modulation with amplitudes of $\sim 5 \times 10^{51}$ erg s$^{-1}$ and $\sim$0.5 MeV for the luminosity and mean energy, respectively, while those values decrease to $\sim 1 \times 10^{51}$ erg s$^{-1}$ and $\sim$0.2 MeV for $\nu_x$. Such a modulation was first discussed in Takiwaki & Kotake (2018) and is associated with the growth of the so-called low-$T/W$ instability (Ott et al. 2005; Watts et al. 2005; Saijo & Yoshida 2006) and the (one-armed) spiral flows. In both of our rotating models, the ratio of rotational to gravitational potential energy after bounce reaches several percent, which is close to the onset of the low-$T/W$ instability. The neutrino spheres of all flavors are located above the PNS core surface at $R \sim 10$ km, where the low-$T/W$ instability starts to (typically) develop, and also below the shock that is deformed by the spiral SASI (for model R1B00). Once the two instabilities appear, they can deform the neutrino spheres and potentially be the origin of the neutrino time modulation (see Kazeroni et al. 2017 for the possible connection of the two instabilities). However, we note that the smaller modulation in the $\nu_x$ signals seems to favor that the outermost $\nu_e$ sphere is more strongly affected by the spiral SASI.

Indeed, there is quantitative evidence that the deformation of the neutrino sphere creates the time-modulated neutrino signals. In Figure 9, we plot spectra of the (angle-dependent) neutrino luminosity $L_{\bar{\nu}_e}$ corresponding to the blue solid line in the top middle panel of Figure 7, of normalized mode amplitudes of the number luminosity $N_{\bar{\nu}_e,m}$ for $m = 1$, 2, and of the normalized mode amplitude of spherical polar expansion of the isodensity surface $R_{11}$ for mode $(\ell, m) = (1, 1)$. Here $N_{\bar{\nu}_e,m}$ is evaluated by

$$N_{\bar{\nu}_e,m} = \frac{\left|\int d\phi N_{\bar{\nu}_e} e^{im\phi}\right|}{\int d\phi N_{\bar{\nu}_e}} \tag{35}$$

at $R = 400$ km and $\theta = 90°$, with $N_\nu$ being the number luminosity estimated in the same way as the luminosity $L_\nu$ (Tamborra et al. 2014). Although we here use the number luminosity $N_\nu$, we can do the same discussion using the luminosity $L_\nu$. $R_{11}$ is the isodensity surface extracted at the rest mass density of $\rho = 10^{11}$ g cm$^{-3}$ corresponding roughly to the neutrino sphere. The normalized mode amplitude of spherical polar expansion of $R_{11}$ is evaluated exactly in the same manner as that of the shock surface. Here we focus on the $\bar{\nu}_e$ signals (120 ms $\leqslant t_{\rm pb} \leqslant$ 180 ms), bearing in mind the detectability (Abbasi et al. 2011; Abe et al. 2016). The detectability for models in this study will be reported elsewhere.

The black line in Figure 9 shows that the time modulation seen in Figure 7 peaks at $F \sim 125$ Hz. This component is mainly composed of $m = 1$ neutrino number flux, as the two peaks of red and black lines are appearing at nearly the same frequency. The peak of $N_{\bar{\nu}_e}$ with $m = 2$, which is a daughter mode of $m = 1$, appears closely at a double frequency $F \sim 240$ Hz of that of $m = 1$ as expected, but the $m = 2$ mode seems to contribute less to the total neutrino signals than the $m = 1$ mode. Finally, as is obvious from the peak at $F \sim 125$ Hz in the green line, the origin of these time modulations of the neutrino signals is $m = 1$ deformation of the neutrino sphere represented by $R_{11}$. We thus conclude that the strong spiral SASI appearing in R1B00 deforms the neutrino sphere with the same $m = 1$ mode and leads to the characteristic neutrino signals.

We also mention that we observe a clear north–south asymmetry in neutrino signals in model R1B12 for $t_{\rm pb} \gtrsim 120$ ms, i.e., between dashed–dotted and dotted red lines, which cannot be seen in the corresponding lines of R1B00. In this model R1B12, the neutrino emission toward the north pole is significantly stronger than the one toward the south. The excess toward the north is consistent with the one-sided explosion to the south pole (see the red line in the top panel of Figure 4 for $A_{10}$ mode). Due to the shock expansion mainly toward the south, the mass accretion is stronger in the northern hemisphere, which results in higher accretion luminosities and neutrino energies in the north pole.

### 3.5. The Role of Neutrino Heating

Next, we make a comparison of the energetics and discuss the role of neutrino heating among the models, particularly how the neutrinos contribute to the shock expansion. In Figure 10, we plot the mass in the gain region $M_{\rm gain}$ (top left); heating rate $\dot{Q}$ (top middle); gain and shock radii $R_{\rm gain}$ and $R_{\rm shock}$, respectively (top right); specific heating rate $\zeta = \dot{Q}/M_{\rm gain}$ (bottom left); heating efficiency $\eta = \dot{Q}/(L_{\nu_e} + L_{\bar{\nu}_e})$, which measures how much of the emergent $\nu_e$ and $\bar{\nu}_e$ contribute to the matter heating (bottom middle); and the ratio of advection to heating timescale $\tau_{\rm adv}/\tau_{\rm heat}$ (bottom right) for each model. To obtain these values, we first define the gain radius $R_{\rm gain}(\theta, \phi)$ at each radial direction $(\theta, \phi)$. $R_{\rm gain}$ is defined at the first point where the net energy deposition rate $\dot{q}$ becomes zero behind the shock, with $\dot{q}$ being defined by

$$\dot{q} \equiv \alpha \sqrt{\gamma} \int d\varepsilon \sum_\nu S^\mu_{(\nu,\varepsilon)} n_\mu. \tag{36}$$

Then, each value is defined by

$$M_{\rm gain} = \int_{R_{\rm gain}(\theta,\phi) < r < R_{\rm shock}(\theta,\phi)} \rho^* dx^3, \tag{37}$$

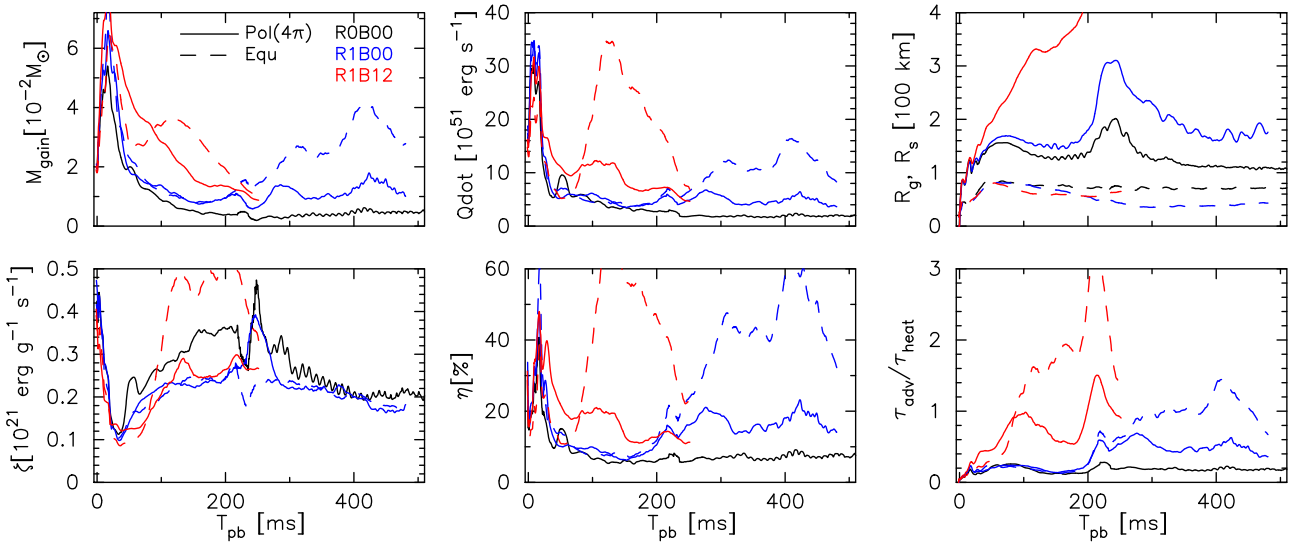


**Figure 10.** We plot $M_{\rm gain}$ (top left), $\dot{Q}$ (top middle), $R_{\rm gain}$ and $R_{\rm shock}$ (top right), $\zeta$ (bottom left), $\eta$ (bottom middle), and $\tau_{\rm adv}/\tau_{\rm heat}$ (bottom right) for each model. See text for their definitions. The solid and dashed lines represent that the volume/surface integral is performed around the polar axis (labeled by "Pol") and equatorial plane (labeled by "Equ"), respectively. Regarding the nonrotating model R0B00, we integrate over all solid angles (solid black line labeled by "4π"). Note that we show half values for extensive variables, i.e., $M_{\rm gain}$ and $\dot{Q}$, for model R0B00 for comparison with other models.

$$\dot{Q} = \int_{R_{\rm gain}(\theta,\phi)<r<R_{\rm shock}(\theta,\phi)} \dot{q} dx^3, \tag{38}$$

$$\tau_{\rm adv} = \frac{M_{\rm gain}}{\left| \int_{r=R_{\rm shock}(\theta,\phi)} \rho^* v^r ds \right|}, \tag{39}$$

and

$$\tau_{\rm heat} = \frac{\int_{R_{\rm gain}(\theta,\phi)<r<R_{\rm shock}(\theta,\phi)} \sqrt{\gamma}\tau dx^3}{\dot{Q}}, \tag{40}$$

where the surface integral $\int ds$ appearing in the denominator of Equation (38) is performed in front of the shock surface and $v^r$ is the radial component of the three-velocity $v^i$. In the top right panel, we show spherical-averaged shock (solid lines) and gain radii (dashed). In the rest of the panels, to illustrate how the values vary relative to the rotational axis, we divide the space into two equal-volume regions, polar and equator, and show the values evaluated in each region. Here we define the polar region (labeled by "Pol") by the cone angle of 60° around the rotational axis, i.e., $\theta \leqslant 60^\circ$ or $\theta \geqslant 120^\circ$, and the equatorial region (labeled by "Equ") by $60^\circ < \theta < 120^\circ$. These ranges are used in the volume and surface integrals in Equations (37)–(40). When we evaluate $\eta(=\dot{Q}/(L_{\nu_e} + L_{\bar{\nu}_e}))$, $\zeta$, and $\tau_{\rm adv}/\tau_{\rm heat}$, we first evaluate every quantity, e.g., $\dot{Q}$ and $L_{\nu_e} + L_{\bar{\nu}_e}$, in each region and then take their ratio. Regarding the model R0B00, we show its values integrated over all solid angles (labeled by "4π") since it has basically no significant angle dependence. Note that we show half values for extensive variables, i.e., $M_{\rm gain}$ and $\dot{Q}$, for model R0B00 to compare with other models.

Figure 10 clearly shows how the rotational and magnetic field effects appear in general and also how they change the values relative to the rotational axis. The (spherically averaged) gain radius is located more inward in rotating models R1B12 (red dashed line in the top right panel) and R1B00 (blue dashed line) than the nonrotating model R0B00 (black dashed line). As can be seen in the top left and top middle panels, the more inward $R_{\rm gain}$ and larger $R_{\rm shock}$ produce a more extended gain region and consequently a larger mass and total heating rate integrated over that region. The nonrotating model R0B00 shows smallest $M_{\rm gain}$ and $\dot{Q}$, typically several times smaller than the other two. The specific heating rate $\zeta$ (bottom left panel) also shows a rotational dependence. In general, R0B00 presents higher $\zeta(=\dot{Q}/M_{\rm gain})$, although $M_{\rm gain}$ and $\dot{Q}$ themselves are smaller than the other two. On the other hand, from the perspective of neutrino heating efficiency, $\eta(=\dot{Q}/(L_{\nu_e} + L_{\bar{\nu}_e}))$ in R0B00 shows the least efficiency (bottom middle). Therefore, rotation works to lower the specific heating rate $\zeta$ but raise the heating efficiency $\eta$. Such a trend is consistent with previous rotating models with detailed neutrino transport in Summa et al. (2018).

In the bottom right panel, all these features mentioned above are aggregated in a value $\tau_{\rm adv}/\tau_{\rm heat}$. Higher $\tau_{\rm adv}/\tau_{\rm heat}$ represents that the dwell time of matter in the gain region is relatively long in terms of heating timescale. It thus leads to a more favorable condition for the explosion. Particularly $\tau_{\rm adv}/\tau_{\rm heat}$ larger than 1 can be a measurement of the onset of runaway shock expansion due to neutrino heating (see Müller et al. 2017; Ott et al. 2018; Summa et al. 2018 for the latest 3D successful explosion models and also O'Connor & Couch 2018 for the 3D nonexplosion models). In the bottom right panel, model R1B12, which has the largest gain region, shows the highest $\tau_{\rm adv}/\tau_{\rm heat}$ (red lines), while model R0B00 shows the lowest value (black line). Therefore, our result also shows that rotation makes $\tau_{\rm adv}/\tau_{\rm heat}$ higher. This tendency is again consistent with Summa et al. (2018). In addition, the magnetic fields also assist the expansion of the shock surface and produce higher $\tau_{\rm adv}/\tau_{\rm heat}$ than the corresponding nonmagnetized model R1B00.

Next, we discuss how rotation affects the energetics in each region relative to the rotational axis. First, in the model R1B00, both $M_{\rm gain}$ and $\dot{Q}$ show significantly higher values along the equator (blue dashed lines) than those in the polar region (blue solid). The blue dashed and solid lines start to diverge when the second shock expansion takes place at $t_{\rm pb} \sim 220$ ms. The

higher values seen in the equatorial region are again due to the rotational shock expansion. These rotational effects were already discussed by Nakamura et al. (2014), though with a very simplified neutrino light bulb method, and we obtain a consistent result in our self-consistent M1 neutrino transport simulations. The heating efficiency $\eta$ in the equatorial region is also nearly twice as high as that in the polar region. As a consequence, $\tau_{\rm adv}/\tau_{\rm heat}$ exceeds 1 only in the equator (blue dashed line) and not in the polar region (blue solid line). If the neutrino heating were more efficient and could actually aid the second shock expansion, it would directly lead to the shock runaway phase. Model R1B00, however, deflates and does not enter the runaway phase during our simulation time up to $t_{\rm pb} \sim 500$ ms.

We see an interesting feature in model R1B12. In this rotating magnetized model, as we have explained in Section 3.2, it exhibits a rapid shock expansion toward the rotational axis soon after core bounce. Therefore, $\tau_{\rm adv}/\tau_{\rm heat}$ in the polar region (red solid line) shows a slightly higher value than the equatorial one (red dashed line). However, the higher value in the red solid line only persists during the first ~100 ms after bounce, and afterward the red dashed line takes over the solid one with largely exceeding 1. Interestingly, $\tau_{\rm adv}/\tau_{\rm heat}$ in the polar region shows basically less than unity until $t_{\rm pb} \sim 200$ ms, although the shock runaway already occurs mainly toward the polar region. The trend is thus completely opposite to that of R1B00, in which the region with larger shock expansion exhibits larger $\tau_{\rm adv}/\tau_{\rm heat}$. We interpret these behaviors as that the neutrino heating is not the main mechanism of the bipolar shock expansion in R1B12, but the magnetic fields play the leading role to aid the shock expansion. On the other hand, as the red dashed line is exceeding unity, the shock expansion along the equator is mainly supported by neutrino heating.

### 3.6. The Asymmetry of Lepton Number Emission

Tamborra et al. (2014) reported the existence of the lepton number emission self-sustained asymmetry (LESA). This phenomenon is characterized by a spherical symmetry breaking of the lepton number emission, basically dominated by a dipole mode. Their analysis exhibited that LESA appears together with a partial distribution of $Y_e$ in the PNS convection zone ($r \sim 25$ km), suggesting that the partial distribution can possibly be the primary cause of LESA. In their subsequent paper (Glas et al. 2019), they also explained the origin of the partial distribution of $Y_e$ by the PNS convection. They showed that the PNS convection excites preferentially the lower-order multipole modes, including the dipole one that drives partial distribution of $Y_e$. In addition, once such a partial distribution of $Y_e$ is fully established, it results in a lepton number emission with a prominent dipole mode that heats more materials on the opposite side to the dipole mode, enhancing a globally deformed shock surface. Consequently, nonspherical mass accretion, basically with low mode $\ell = 1$, onto the PNS core surface continues to replenish the lepton-rich matter and sustains the partial distribution of $Y_e$ (Tamborra et al. 2014).

O'Connor & Couch (2018) and Vartanyan et al. (2019b) also reported the appearance of LESA using the M1 neutrino transport method, i.e., full multi-D neutrino transport. O'Connor & Couch (2018) pointed out the importance of velocity-dependent terms in the neutrino transport, as the models without that term do not show any conclusive evidence for LESA. Vartanyan et al. (2019b) also showed that the dipole mode can be comparable to the monopole one in the late postbounce phase $t_{\rm pb} \sim 650$ ms. Therefore, although the growth rate of dipole magnitude may actually depend on the detailed neutrino transport scheme (Glas et al. 2019), the LESA seems to be a common phenomenon in CCSNe.

Following O'Connor & Couch (2018) and Vartanyan et al. (2019b), we plot the ratio of monopole to dipole mode of the lepton number emission as a function of the postbounce time in Figure 11. To plot the figure, we first evaluate the net lepton number flux via neutrinos $\mathcal{L}_\nu \equiv \mathcal{L}_{\nu_e} - \mathcal{L}_{\bar{\nu}_e}$ at $r = 400$ km and then obtain the coefficient $\mathcal{L}_{\ell m}$ of spherical polar expansion of $\mathcal{L}_\nu$ as we do in Figure 4. In the top panel, we plot the dipole magnitude $|\mathcal{L}_1|$ normalized by the monopole one $\mathcal{L}_0$, where we take the following definition (O'Connor & Couch 2018):

$$|\mathcal{L}_1| \equiv 3\sqrt{\sum_{m=-1}^{1}\mathcal{L}_{1m}^2}. \quad (41)$$

In the lower three panels, we plot the value $3\mathcal{L}_{1m}/\mathcal{L}_0$ for each quantum number $m$ in each model to discuss the correlation with the shock morphology.

From the top panel, we see that the absolute magnitude of the normalized dipole mode in model R1B12 shows a significantly larger value than the other two nonexplosion models. In this model R1B12, the dominant contribution to the total dipole mode is mainly coming from $m = 0$ mode (blue line in the second panel). Since it basically exhibits the positive value for $t_{\rm pb} \gtrsim 100$ ms, the relative $\bar{\nu}_e$'s number flux is less toward positive $z$-axis and higher toward negative $z$-axis. From Figure 4, the shock morphology with $(\ell, m) = (1, 0)$ mode becomes stronger for $t_{\rm pb} \gtrsim 100$ ms with a negative value that reflects that the shock expansion takes place relatively stronger toward the negative $z$-axis (also see the final snapshot of the shock morphology in Figure 1). It is thus opposite to the dipole mode of the lepton number flux.

Although the anticorrelation between the orientation of the excess of the lepton number emission (positive $z$-axis) and the shock expansion (negative $z$-axis) seen in model R1B12 is consistent with the mechanism of LESA, the highest value ~0.4 (red line in top panel) is significantly smaller than the values of Tamborra et al. (2014), in which they find the excess of dipole mode in all models irrespective of the explosion. Therefore, to see if LESA is actually the mechanism of the excited dipole mode of the lepton number emission in model R1B12, we show in Figure 12 the distribution of $Y_e$ in the PNS at four different time slices $T_{\rm pb} = 144$ (top left), 205 (top right), 225 (bottom left), and 251 ms (bottom right). In addition, we also show the distribution on $x$-$y$ (bottom left), $x$-$z$ (top left), and $y$-$z$ (top right) planes in every minipanel. We note that, from the first and second panels in Figure 11, the strong excess of lepton number emission mainly orienting toward positive $z$-axis is observed for $T_{\rm pb} \gtrsim 100$ ms. Therefore, if LESA is the origin of the excess, we would expect that the partial distribution of $Y_e$ has a dipole mode that orients opposite to the excess (see the schematic Figure 15 in Tamborra et al. 2014), i.e., toward the positive $z$-axis in model R1B12.

From the $Y_e$ distribution at $T_{\rm pb} = 144$ and 205 ms, we do not see any clear dipole-like structure of $Y_e$ on the $x$-$z$ and $y$-$z$ planes. A clear dipole-like structure appears only near the end of the simulation time (see bottom two panels, $T_{\rm pb} \gtrsim 225$ ms). The reason for the apparent inconsistency, namely, the dipole lepton number emission without the existence of noticeable partial distribution of $Y_e$, can be understood from Tamborra et al. (2014). According to their study, the dipole emission of

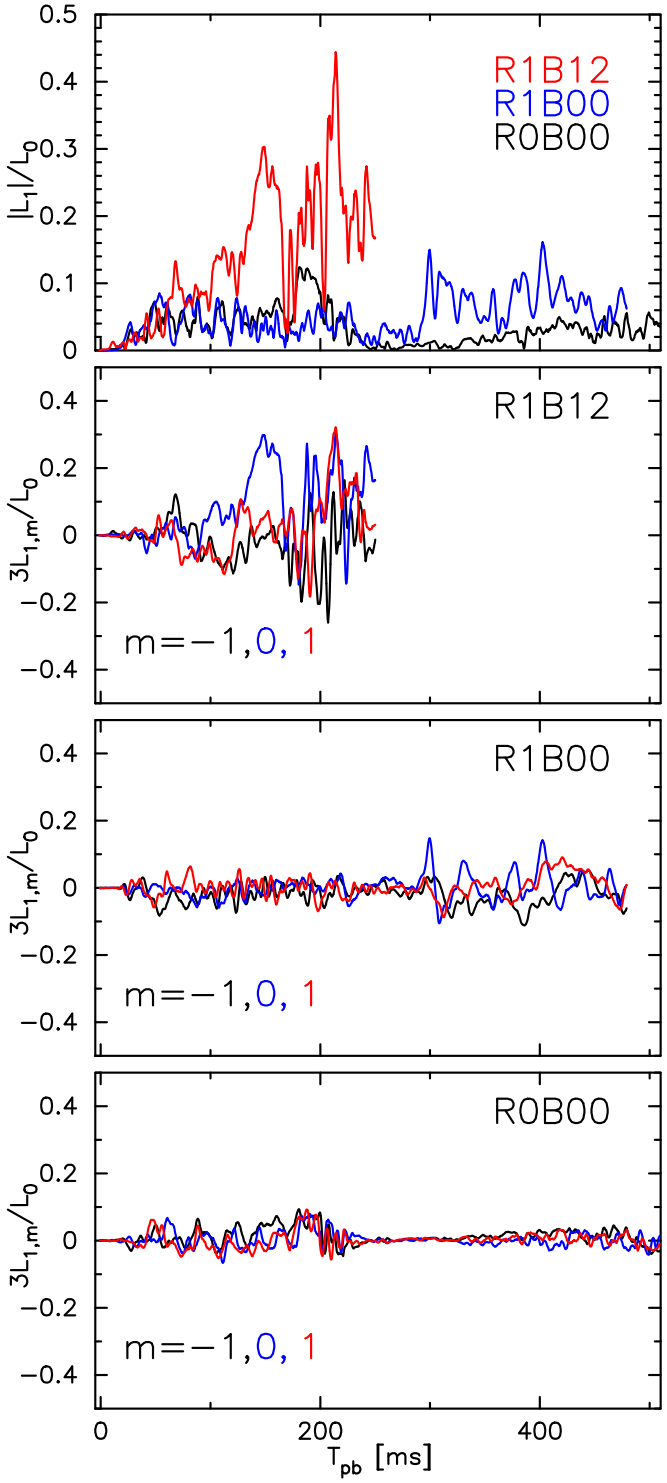


**Figure 11.** Normalized dipole magnitude (top panel) and contributions from each quantum number $m$ for each model (bottom threes). In the top panel, the color represents the model name, while it indicates the quantum number $m = 0, \pm 1$ in other plots. We can see that model R1B12 (red line in the top panel) shows a clear excess in its dipole magnitude.

total lepton number is produced mainly at two different regions, the PNS convection zone $R \lesssim 20$ km, where the main dipole emission (∼70%–80%) occurs, and the entropy-driven convection zone several 10 km $\lesssim R \lesssim R_{\rm shock}$, where the dipole emission reaches its asymptotic value. At the latter location, the partial distribution of $Y_e$ is established mainly by a replenishment of rich $Y_e$ material that is transported with stellar mantle deflected by the deformed shock surface.

Figure 13 shows the radial profile of the total lepton number flux $\mathcal{L}_\nu (=\mathcal{L}_{\nu_e} - \mathcal{L}_{\bar{\nu}_e})$ at three representative time slices $T_{\rm pb} = 144$ (solid lines), 205 (dashed), and 251 ms (dotted). Here $\mathcal{L}_\nu$ is a hemispheric integration of the total lepton number flux measured in the comoving frame. The hemispheric integration is performed for northern and southern hemispheres, where we observe the excess and reduction of asymptotic $\mathcal{L}_\nu$, respectively. By comparing the red and black lines at each time slice, they are almost overlapping just above the PNS convection zone $R \sim 20$ km, while the difference gradually appears with radius especially at $R \gtrsim 50$ km, i.e., in the entropy-driven convection zone. Such a profile, namely, the minor contribution from the PNS convection zone to the dipole emission, is completely different from the one in Tamborra et al. (2014), which shows that a larger difference than ours already appears at $R \sim 20$ km. We therefore conclude that the dipole emission seen in model R1B12 did not originate from LESA but from the accretion-induced partial distribution of $Y_e$ above the PNS convection zone.

## 4. Discussion and Conclusions

We have presented the first 3D–GR MHD simulations of a 20 $M_\odot$ star with spectral neutrino transport. For the nuclear EOS and neutrino opacities, we used SFHo of Steiner et al. (2013) and a baseline set of weak interactions (Bruenn 1985; Rampp & Janka 2002), where nucleon–nucleon bremsstrahlung is additionally taken into account, respectively. Neutrino transport is handled by the M1 closure scheme with the red and Doppler shift terms being fully considered.

We calculated three models, nonrotating nonmagnetized, rotating nonmagnetized, and rotating magnetized, to explore the effects of a progenitor's rotation and magnetic field on both the dynamics and neutrino profiles. Regarding the dynamics, while no shock revival was observed in two nonmagnetized models during our simulation times, the shock expansion initiated shortly after bounce in a rotating magnetized model. Initially the shock morphology takes a bipolar structure, which was eventually taken over by a unipolar one. The shock front reached 1000 km at $t_{\rm pb} \sim 220$ ms and still continued expansion at the end of our simulation time. From our analysis for the rotating magnetized model, we interpreted that the polar expansion is driven mainly by the magnetic pressure, while the equatorial expansion is facilitated by the neutrino heating. Although we did not see the shock revival in two nonmagnetized models, the standing shock is located further outward in the rotating model, which expands the gain region and increases the mass in the region. Therefore, we obtained a consistent result with previous studies that the (moderate) rotation makes the condition more favorable for the explosion than the nonrotating case.

Using the same (or very similar) nonrotating 20 $M_\odot$ progenitor star as in this study, some previous 3D studies have shown a successful explosion (Melson et al. 2015; Ott et al. 2018; Burrows et al. 2019), while others have not (Tamborra et al. 2014; Melson et al. 2015; O'Connor & Couch 2018). It is thus worth comparing our nonrotating and nonexploding model R0B00 with these previous studies. One of the major limitations in this work is its relatively lower numerical resolution compared to the previous ones. It has been thoroughly examined that insufficient resolution can potentially

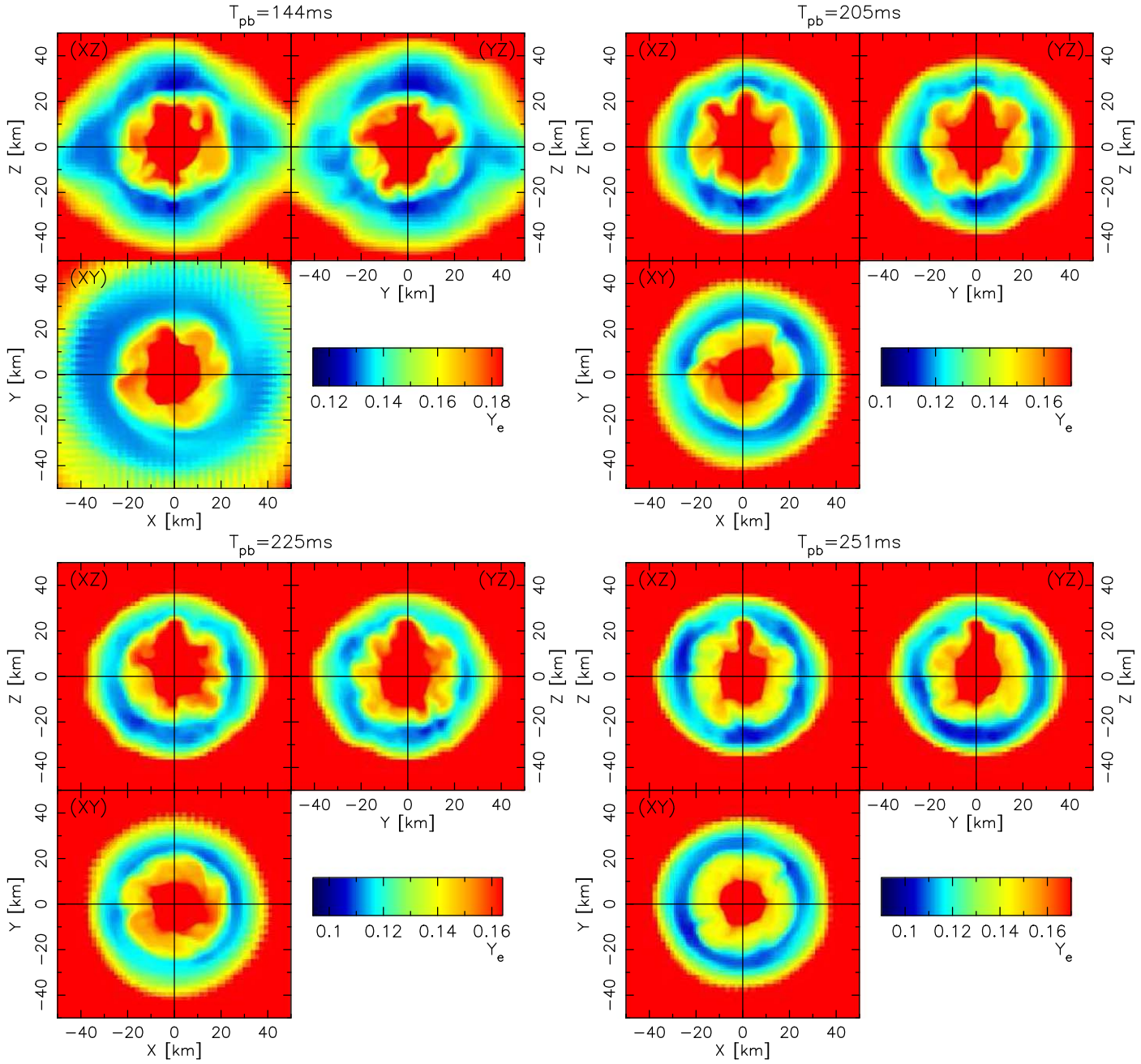


**Figure 12.** Distribution of $Y_e$ in the PNS at four different time slices $T_{\rm pb} = 144$ (top left), 205 (top right), 225 (bottom left), and 251 ms (bottom right). In each panel, there are three minipanels that depict $x$-$y$ (bottom left), $x$-$z$ (top left), and $y$-$z$ (top right) planes. Although the partial distribution of $Y_e$ seemingly with higher-order modes is visible initially (say, $T_{\rm pb} = 144$ and 205 ms; top two panels), we cannot see any clear dipole-like structure. At around the end of our simulation time ($T_{\rm pb} \gtrsim 220$ ms), the dipole mode seems to gradually grow with orienting toward positive $z$-axis. The structure is not destroyed by the PNS convection and persists at least for a few tens of milliseconds until the end of our simulation time in model R1B12.

inhibit the shock revival due to less turbulent pressure (e.g., Couch & Ott 2015; Müller & Janka 2015; Roberts et al. 2016; Takiwaki et al. 2016; Burrows et al. 2019; Nagakura et al. 2019). For instance, Ott et al. (2018) performed full relativistic 3D calculations with M1 neutrino transport and obtained the shock revival. This might be possibly due to their higher numerical resolution within the shock surface that achieves a factor of $\sim$2–4 higher than ours. The higher numerical resolution allows the growth of turbulence, leading to an additional pressure support. It should be also noted that more up-to-date neutrino opacities, e.g., a strangeness-dependent contribution to the axial-vector coupling constant or many-body corrections to neutrino-nucleon scattering (Burrows & Sawyer 1998; Horowitz et al. 2017), generally benefit in facilitating the shock revival (e.g., Kotake et al. 2018; Burrows et al. 2019). We are currently conducting CCSN simulations with better neutrino opacities following Kotake et al. (2018), which will be reported elsewhere in the near future.

We investigated the effect of the precollapse rotation and magnetic fields on the neutrino signals. In general, both of the rotation and magnetic fields decrease the neutrino luminosity and energy, as they make the PNS core less compact owing to the centrifugal force and/or mass ejection. In addition, the rotation produces angle-dependent neutrino signals relative to

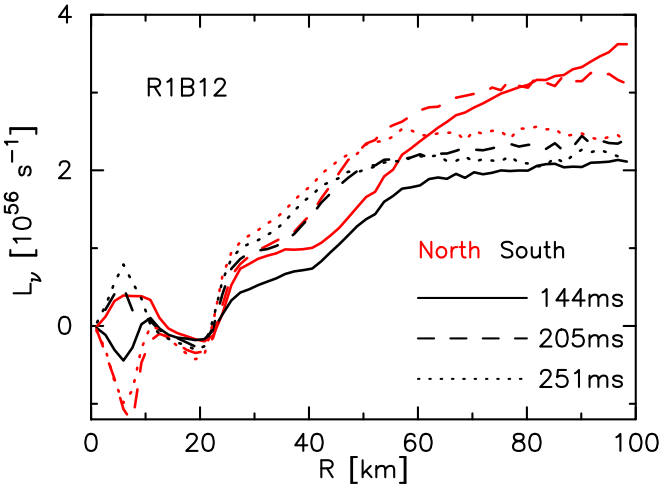


**Figure 13.** Radial profile of the total lepton number flux $\mathcal{L}_\nu(=\mathcal{L}_{\nu_e} - \mathcal{L}_{\bar{\nu}_e})$ at three representative time slices $T_{\rm pb} = 144$ (solid lines), 205 (dashed), and 251 ms (dotted). We plot $\mathcal{L}_\nu$ integrated over the northern (red lines) and southern (black) hemispheres at a given radius $R$. Here, from Figure 11, the northern (southern) hemisphere corresponds to where we observe the excess (reduction) of $\mathcal{L}_\nu$, i.e., with relatively higher $\nu_e(\bar{\nu}_e)$ number flux.

the rotational axis. The neutrino luminosity and energy along the equator are significantly lower than those along the rotational axis. We observed a quasi-periodic time modulation in the neutrino signals, especially in model R1B00 toward the equator, that is greatly suppressed along the rotational axis. From our spectral analysis, the peak frequencies of the time-modulated signals and of the $m = 1$ deformation of neutrino sphere(s) have nearly the same value. Therefore, together with the less modulation in heavier-type neutrino signals, we consider that the spiral SASI mode deforms the neutrino spheres, leading to the quasi-periodic signals. Our results showed clear dependencies of neutrino signals on the progenitor's rotation, magnetic field, and observation angle. A more systematic study (such as changing the progenitor model, the initial MR strength, and the inclination between the rotation and magnetic axis) is needed for clarifying the multi-messenger signals from MR-driven CCSNe.

We also witnessed the dipole emission of lepton number for our MR explosion model, albeit weak. Although it is similar to the LESA phenomenon (Tamborra et al. 2014; O'Connor & Couch 2018; Glas et al. 2019; Vartanyan et al. 2019b), from our detailed analysis on the $Y_e$ distribution in the PNS convection layer and also on the spatial origin of dipole emission, we found that it is not associated with LESA. We consider that the strong unipolar explosion in model R1B12 supplies rich $Y_e$ material on one side and produces the partial distribution leading to the dipole emission from the entropy-driven convection zone. We, however, stress that more MHD simulations with sophisticated neutrino transport are indeed necessary to mention the robustness of the unipolar explosion seen in our model R1B12 and of the dipole emission associated with it.

As an important 3D effect, we showed that the kink instability is most likely to appear in the magnetized model that can potentially broaden the expanding blob, leading to weaker bipolar jets. However, the PNS core may also be subject to the low-$T/W$ instability; we could not disentangle the outcomes of these two possibly coexisting instabilities. Further numerical simulations by other independent groups, preferably with finer numerical resolutions, are definitely required to clarify the interplay between the two instabilities.

In the end of our discussion, we briefly mention the possible role of MRI. Although the stellar magnetic field configuration and its strength at precollapse phase are poorly understood, strong initial magnetic fields of $\sim 10^{12}$ G as employed in this study might be too strong according to magnetized stellar evolution calculations by Heger et al. (2005), which give $\lesssim 10^9$ G (but also see Peres et al. 2019, for a possible scenario for considerably stronger initial magnetic fields). To see how the MRI amplifies such plausibly weak magnetic fields, Obergaulinger et al. (2009) conducted local shearing disk simulations. Their results showed that the initial seed magnetic fields inside the PNS $\mathcal{O}(10^{12})$ G can be amplified to dynamically relevant strengths $\mathcal{O}(10^{15})$ G within several milliseconds. Since the main magnetic field amplification mechanism during core collapse is compression, their initial seed magnetic fields inside the PNS $\mathcal{O}(10^{12})$ G could originate from the precollapse phase $\mathcal{O}(10^9)$ G, which seems compatible with the stellar evolution calculation.

Sawai & Yamada (2014) have shown in their global 2D axisymmetric simulations that the MRI can not only amplify the initial seed magnetic fields but also produce a global magnetic field in the postshock region. Later, a globally ordered field amplification in the PNS was found in full 3D–GR MHD simulations by Mösta et al. (2014). Furthermore, Raynaud et al. (2020) just recently reported the first numerical evidence of generation of magnetic fields inside the PNS convection zone with dynamically relevant strengths $\mathcal{O}(10^{15})$ G irrespective of the initial seed magnetic field strengths. All these facts indicate that model R1B12 in this study is not too extreme but might be plausible, although the typical length scale of the MRI $\lesssim \mathcal{O}(10)$ m is far too small to resolve by our current numerical grid size (simply limited by our currently available computational resources). Other than the MR explosion scenario, the turbulence in the MRI could enhance the neutrino heating efficiency, which could impact the neutrino mechanism (Sawai & Yamada 2014; Masada et al. 2015). All these subjects remain to be studied. As such, we can see a vast untouched (research) territory lying in front of us, into which we have just made a first jump with a newly developed tool (our 3D–GR MHD code) in hand.

We thank Shota Shibagaki, Martin Obergaulinger, and Federico Maria Guercilena for helpful discussions and useful comments. We also acknowledge H.-T. Janka for his valuable comments on the dipole emission of lepton number. This research was supported by the ERC Starting Grant EUROPIUM-677912 (T.K. and A.A.); JSPS KAKENHI grant Nos. JP17H05206, JP17K14306, JP17H01130, JP17H06364, and JP18H01212 (K.K. and T.T.); and JICFuS as a priority issue to be tackled by using the Post "K" Computer. Numerical computations were carried out on Cray XC50 at CfCA, NAOJ.

## Appendix

In this appendix, we show that our metric evolution implementation has a fourth-order convergence in space by checking the well-known polarized Gowdy wave test (Alcubierre et al. 2004). We omit to write the Gowdy wave metric and initial condition that can be found elsewhere (e.g., Alcubierre et al. 2004). We evolve the collapsing Gowdy

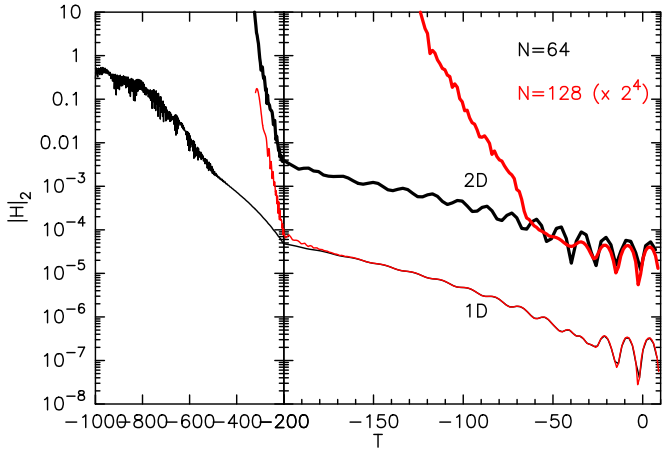


**Figure A1.** $L_2$ norm of violation of the Hamiltonian constraint $|\mathcal{H}|_2$ for the coarser spacing model with $N = 64$ (black lines) and finer ones with 128 (red). For finer-resolution models (red lines), we multiply $|\mathcal{H}|_2$ by $2^4$, since we use fourth-order spatial finite differencing. We evolve the metric backward in time starting at $T \sim 9.875$.

wave metric backward in time using the harmonic slicing condition with zero shift vector $\beta^i = 0$ as for the gauge condition. Although the Gowdy wave is a plane wave, we perform the test in both full 1D and 2D space. In the latter 2D case, we tilt the propagation direction of the plane wave at 45° in the $x$-$y$ plane. We employ two different grid spacings $dx = 1/N$ with $N = 64$ or 128 to check for the numerical convergence. Figure A1 shows the $L_2$ norm of violation of the Hamiltonian constraint $|\mathcal{H}|_2$ for the coarser spacing model with $N = 64$ (black line) and the finer one with 128 (red). For finer-resolution models (red lines), we multiply $|\mathcal{H}|_2$ by $2^4$, since we use fourth-order spatial finite differencing. From the figure, we see that there is almost a perfect overlap during the first ∼180 and ∼40 crossing times in the 1D and 2D tests, respectively, which shows that our metric evolution scheme actually achieves a fourth-order convergence in space.

## ORCID iDs

Takami Kuroda https://orcid.org/0000-0001-5168-6792
Almudena Arcones https://orcid.org/0000-0002-6995-3032
Tomoya Takiwaki https://orcid.org/0000-0003-0304-9283
Kei Kotake https://orcid.org/0000-0003-2456-6183

## References

Abbasi, R., Abdou, Y., Abu-Zayyad, T., et al. 2011, A&A, 535, A109
Abdikamalov, E., Ott, C. D., Radice, D., et al. 2015, ApJ, 808, 70
Abe, K., Abe, Ke., Aihara, H., et al. 2016, KEK Preprint 2016-21, https://lib-extopc.kek.jp/preprints/PDF/2016/1627/1627021.pdf
Akiyama, S., Wheeler, J. C., Meier, D. L., & Lichtenstadt, I. 2003, ApJ, 584, 954
Alcubierre, M., Allen, G., Bona, C., et al. 2004, CQGra, 21, 589
Antón, L., Zanotti, O., Miralles, J. A., et al. 2006, ApJ, 637, 296
Ardeljan, N. V., Bisnovatyi-Kogan, G. S., & Moiseenko, S. G. 2000, A&A, 355, 1181
Baumgarte, T. W., & Shapiro, S. L. 1999, PhRvD, 59, 024007
Begelman, M. C. 1998, ApJ, 493, 291
Bethe, H. A., & Wilson, J. R. 1985, ApJ, 295, 14
Bisnovatyi-Kogan, G. S. 1970, AZh, 47, 813
Blandford, R. D., & Znajek, R. L. 1977, MNRAS, 179, 433
Blondin, J. M., & Mezzacappa, A. 2007, Natur, 445, 58
Bollig, R., Janka, H.-T., Lohs, A., et al. 2017, PhRvL, 119, 242702
Bruenn, S. W. 1985, ApJS, 58, 771
Burrows, A. 2013, RvMP, 85, 245
Burrows, A., Dessart, L., Livne, E., Ott, C. D., & Murphy, J. 2007, ApJ, 664, 416
Burrows, A., Dolence, J. C., & Murphy, J. W. 2012, ApJ, 759, 5
Burrows, A., Radice, D., Vartanyan, D., et al. 2019, MNRAS, 485, 3153
Burrows, A., & Sawyer, R. F. 1998, PhRvC, 58, 554
Colella, P., & Woodward, P. R. 1984, JCoPh, 54, 174
Couch, S. M. 2013, ApJ, 775, 35
Couch, S. M., & Ott, C. D. 2015, ApJ, 799, 5
Dimmelmeier, H., Font, J. A., & Müller, E. 2002, A&A, 388, 917
Dolence, J. C., Burrows, A., Murphy, J. W., & Nordhaus, J. 2013, ApJ, 765, 110
Evans, C. R., & Hawley, J. F. 1988, ApJ, 332, 659
Foglizzo, T., Kazeroni, R., Guilet, J., et al. 2015, PASA, 32, e009
Foglizzo, T., Scheck, L., & Janka, H.-T. 2006, ApJ, 652, 1436
Fryer, C. L., & Warren, M. S. 2004, ApJ, 601, 391
Gammie, C. F., McKinney, J. C., & Tóth, G. 2003, ApJ, 589, 444
Glas, R., Janka, H. T., Melson, T., Stockinger, G., & Just, O. 2019, ApJ, 881, 36
Hanke, F., Marek, A., Müller, B., & Janka, H.-T. 2012, ApJ, 755, 138
Hanke, F., Müller, B., Wongwathanarat, A., Marek, A., & Janka, H.-T. 2013, ApJ, 770, 66
Hannestad, S., & Raffelt, G. 1998, ApJ, 507, 339
Harada, A., Nagakura, H., Iwakami, W., et al. 2019, ApJ, 872, 181
Harten, A., Lax, P. D., & Leer, B. v. 1983, SIAMR, 25, 35
Hawke, I., Löffler, F., & Nerozzi, A. 2005, PhRvD, 71, 104006
Heger, A., & Langer, N. 2000, ApJ, 544, 1016
Heger, A., Woosley, S. E., & Spruit, H. C. 2005, ApJ, 626, 350
Horowitz, C. J., Caballero, O. L., Lin, Z., O'Connor, E., & Schwenk, A. 2017, PhRvC, 95, 025801
Iwamoto, K., Mazzali, P. A., Nomoto, K., et al. 1998, Natur, 395, 672
Janka, H.-T., Melson, T., & Summa, A. 2016, ARNPS, 66, 341
Just, O., Bollig, R., Janka, H. T., et al. 2018, MNRAS, 481, 4786
Kazeroni, R., Guilet, J., & Foglizzo, T. 2017, MNRAS, 471, 914
Kitaura, F. S., Janka, H.-T., & Hillebrandt, W. 2006, A&A, 450, 345
Kotake, K., Sato, K., & Takahashi, K. 2006, RPPh, 69, 971
Kotake, K., Takiwaki, T., Fischer, T., Nakamura, K., & Martínez-Pinedo, G. 2018, ApJ, 853, 170
Kotake, K., Takiwaki, T., Suwa, Y., et al. 2012, AdAst, 2012, 428757
Kotake, K., Yamada, S., & Sato, K. 2003, PhRvD, 68, 044023
Kuroda, T., Kotake, K., & Takiwaki, T. 2012, ApJ, 755, 11
Kuroda, T., Kotake, K., & Takiwaki, T. 2016a, ApJL, 829, L14
Kuroda, T., Takiwaki, T., & Kotake, K. 2014, PhRvD, 89, 044011
Kuroda, T., Takiwaki, T., & Kotake, K. 2016b, ApJS, 222, 20
Kuroda, T., & Umeda, H. 2010, ApJS, 191, 439
LeBlanc, J. M., & Wilson, J. R. 1970, ApJ, 161, 541
Lentz, E. J., Bruenn, S. W., Hix, W. R., et al. 2015, ApJL, 807, L31
Li, L.-X. 2000, ApJL, 531, L111
Liebendörfer, M., Mezzacappa, A., Thielemann, F.-K., et al. 2001, PhRvD, 63, 103004
Lyubarskii, Y. E. 1999, MNRAS, 308, 1006
Maeda, K., Kawabata, K., Mazzali, P. A., et al. 2008, Sci, 319, 1220
Marek, A., & Janka, H.-T. 2009, ApJ, 694, 664
Marronetti, P., Tichy, W., Brügmann, B., González, J., & Sperhake, U. 2008, PhRvD, 77, 064010
Masada, Y., Takiwaki, T., & Kotake, K. 2015, ApJL, 798, L22
McKinney, J. C. 2006, MNRAS, 368, 1561
Meier, D. L., Epstein, R. I., Arnett, W. D., & Schramm, D. N. 1976, ApJ, 204, 869
Melson, T., Janka, H.-T., Bollig, R., et al. 2015, ApJL, 808, L42
Mikami, H., Sato, Y., Matsumoto, T., & Hanawa, T. 2008, ApJ, 683, 357
Mirizzi, A., Tamborra, I., Janka, H.-T., et al. 2016, NCimR, 39, 1
Mösta, P., Richers, S., Ott, C. D., et al. 2014, ApJL, 785, L29
Müller, B. 2016, PASA, 33, e048
Müller, B., & Janka, H.-T. 2015, MNRAS, 448, 2141
Müller, B., Janka, H.-T., & Marek, A. 2012, ApJ, 756, 84
Müller, B., Melson, T., Heger, A., & Janka, H.-T. 2017, MNRAS, 472, 491
Müller, E., & Hillebrandt, W. 1979, A&A, 80, 147
Nagakura, H., Burrows, A., Radice, D., & Vartanyan, D. 2019, MNRAS, 490, 4622
Nagakura, H., Burrows, A., Radice, D., & Vartanyan, D. 2020, MNRAS, 492, 5764
Nakamura, K., Kuroda, T., Takiwaki, T., & Kotake, K. 2014, ApJ, 793, 45
Narayan, R., Li, J., & Tchekhovskoy, A. 2009, ApJ, 697, 1681
Obergaulinger, M., & Aloy, M. Á 2017, MNRAS, 469, L43
Obergaulinger, M., & Aloy, M. Á 2020, MNRAS, 492, 4613

Obergaulinger, M., Cerdá-Durán, P., Müller, E., & Aloy, M. A. 2009, A&A, 498, 241
Obergaulinger, M., Janka, H.-T., & Aloy, M. A. 2014, MNRAS, 445, 3169
O'Connor, E. P., & Couch, S. M. 2018, ApJ, 865, 81
Ott, C. D., Burrows, A., Dessart, L., & Livne, E. 2008, ApJ, 685, 1069
Ott, C. D., Ou, S., Tohline, J. E., & Burrows, A. 2005, ApJL, 625, L119
Ott, C. D., Roberts, L. F., da Silva Schneider, A., et al. 2018, ApJL, 855, L3
Pan, K.-C., Liebendörfer, M., Couch, S. M., & Thielemann, F.-K. 2018, ApJ, 857, 13
Peres, I., Sabach, E., & Soker, N. 2019, MNRAS, 486, 1652
Powell, J., & Müller, B. 2019, MNRAS, 487, 1178
Radice, D., Abdikamalov, E., Ott, C. D., et al. 2018, JPhG, 45, 053003
Rampp, M., & Janka, H.-T. 2002, A&A, 396, 361
Raynaud, R., Guilet, J., Janka, H.-T., & Gastine, T. 2020, SciA, 6
Rembiasz, T., Obergaulinger, M., Cerdá-Durán, P., Müller, E., & Aloy, M. A. 2016, MNRAS, 456, 3782
Roberts, L. F., Ott, C. D., Haas, R., et al. 2016, ApJ, 831, 98
Saijo, M., & Yoshida, S. 2006, MNRAS, 368, 1429
Sawai, H., & Yamada, S. 2014, ApJL, 784, L10
Scheck, L., Kifonidis, K., Janka, H. T., & Müller, E. 2006, A&A, 457, 963
Scheidegger, S., Käppeli, R., Whitehouse, S. C., Fischer, T., & Liebendörfer, M. 2010, A&A, 514, A51
Shibata, M., Kiuchi, K., Sekiguchi, Y., & Suwa, Y. 2011, PThPh, 125, 1255
Shibata, M., & Nakamura, T. 1995, PhRvD, 52, 5428
Shibata, M., & Sekiguchi, Y.-I. 2005, PhRvD, 72, 044014
Steiner, A. W., Hempel, M., & Fischer, T. 2013, ApJ, 774, 17
Sumiyoshi, K., & Yamada, S. 2012, ApJS, 199, 17
Sumiyoshi, K., Yamada, S., Suzuki, H., et al. 2005, ApJ, 629, 922
Summa, A., Janka, H.-T., Melson, T., & Marek, A. 2018, ApJ, 852, 28
Takiwaki, T., & Kotake, K. 2018, MNRAS, 475, L91
Takiwaki, T., Kotake, K., & Sato, K. 2009, ApJ, 691, 1360
Takiwaki, T., Kotake, K., & Suwa, Y. 2014, ApJ, 786, 83
Takiwaki, T., Kotake, K., & Suwa, Y. 2016, MNRAS, 461, L112
Tamborra, I., Hanke, F., Janka, H.-T., et al. 2014, ApJ, 792, 96
Tamborra, I., Hanke, F., Müller, B., Janka, H.-T., & Raffelt, G. 2013, PhRvL, 111, 121104
Tanaka, M., Kawabata, K. S., Maeda, K., et al. 2009, ApJ, 699, 1119
Tomimatsu, A., Matsuoka, T., & Takahashi, M. 2001, PhRvD, 64, 123003
Vartanyan, D., Burrows, A., & Radice, D. 2019a, MNRAS, 489, 2227
Vartanyan, D., Burrows, A., Radice, D., Skinner, M. A., & Dolence, J. 2019b, MNRAS, 482, 351
Walk, L., Tamborra, I., Janka, H.-T., & Summa, A. 2019, PhRvD, 100, 063018
Watts, A. L., Andersson, N., & Jones, D. I. 2005, ApJL, 618, L37
White, C. J., Stone, J. M., & Gammie, C. F. 2016, ApJS, 225, 22
Wilson, J. R. 1985, in Numerical Astrophysics, ed. J. M. Centrella, J. M. Leblanc, & R. L. Bowers (Boston, MA: Jones and Bartlett), 422
Winteler, C., Käppeli, R., Perego, A., et al. 2012, ApJL, 750, L22
Woosley, S. E., & Heger, A. 2007, PhR, 442, 269
Yoshida, T., Takiwaki, T., Kotake, K., et al. 2019, ApJ, 881, 16
Zlochower, Y., Baker, J. G., Campanelli, M., & Lousto, C. O. 2005, PhRvD, 72, 024021